國立臺灣大學電機資訊學院電信工程學研究所

碩士論文

Graduate Institute of Communication Engineering
College of Electrical Engineering and Computer Science
National Taiwan University

Master's Thesis

採用多衛星跨軌干涉合成孔徑雷達偵測內波

Internal Wave Detection with Multi-Satellite Cross-Track InSAR Imaging

王通晟

Tung-Cheng Wang

指導教授：江簡富 博士

Advisor: Jean-Fu Kiang, Ph.D.

中華民國 113 年 7 月

July 2024

doi:10.6342/NTU202501333

國立臺灣大學碩士學位論文
口試委員會審定書
MASTER'S THESIS ACCEPTANCE CERTIFICATE
NATIONAL TAIWAN UNIVERSITY

採用多衛星跨軌干涉合成孔徑雷達偵測內波

Internal Wave Detection with Multi-Satellite Cross-Track InSAR Imaging

本論文係 王通晟 (姓名) R08942031 (學號)在國立臺灣大學電信工程學研究所 (系/所/學位學程)完成之碩士學位論文，於民國 113 年 7 月 15 日承下列考試委員審查通過及口試及格，特此證明。

The undersigned, appointed by the Institute of Graduate Institute of Communication Engineering on 15 (date) July (month) 2024 (year) have examined a Master's thesis entitled above presented by Tung-Cheng Wang (name) R08942031 (student ID) candidate and hereby certify that it is worthy of acceptance.

口試委員 Oral examination committee:

江簡富　　李翔傑　　丁建均

（指導教授 Advisor）

所長 Director: 張宏宇

Acknowledgment

First of all, I would like to express my sincerest thanks to my thesis advisor, Professor Jean-Fu Kiang, for his advice and support throughout the past six years to pursue my master's degree. His unwavering patience, enthusiastic attitude, and research experiences motivate me to enhance my understanding on electromagnetic theories and their applications and, hopefully, to be a better researcher. I am also grateful to my thesis readers, Professor Jian-Jiun Ding and Professor Hsiang-Chieh Lee, for their valuable comments to improve the quality of this thesis. I would like to thank the faculty in the Department of Electrical Engineering and the Graduate Institute of Communication Engineering, National Taiwan University, for many useful courses they offered. My classmate in graduate school, my partner, and my friends are also appreciated for their friendship, companionship, and emotional support throughout these years. The deepest appreciations are owed to my family for their considerations and encouragement, and to the deities I worship, represented by Un-chú-kong and Má-chó͘. They always support me to pursue this master degree, and I am pleased to share this honor with them.

doi:10.6342/NTU202501333

中文摘要

內波易對水下行動產生威脅，但由於其在水面上的足跡易被風浪掩埋，即時偵測很困難。本論文使用多衛星跨軌干涉合成孔徑雷達成像 (multi-satellite cross-track interferometric synthetic aperture radar) 技術，獲取內波在水面上的足跡。多組衛星以不同方向、海拔飛行，將獲取的海面高度影像作平均，以消除周遭風浪的影響，但水平方向的解析度因此變差。本論文參照三起內波事件進行模擬，輔以適當參數與運作情境，可在風速每秒六公尺內達到水平方向解析度 14 公尺，海面高度誤差則在公分等級。

關鍵字：跨軌干涉合成孔徑雷達、內波、水面足跡、多組衛星

doi:10.6342/NTU202501333

Abstract

Internal waves, which can wreak havoc on underwater activities, are difficult to detect because their signatures on the sea surface are easily obscured by wind waves. In this work, a cross-track interferometric synthetic aperture radar (XTI-SAR) imaging technique based on multiple satellite-pairs is proposed to detect the surface signatures of internal wave, with higher height accuracy and finer horizontal resolution that can be achieved by using conventional satellite pair. By superposing the XTI-SAR images acquired from multiple satellite pairs, random features of wind waves are filtered out to reveal the surface signatures of internal wave, without compromising the horizontal resolution. Three internal-wave events are simulated to demonstrate the efficacy of the proposed approach, with height accuracy of centimeters and spatial resolution of 14 m, under wind speed of $U_{10} \leq 6$ m/s.

Keywords: cross-track interferometric synthetic aperture radar (XTI-SAR), internal wave, surface signature, multiple satellite pairs.

doi:10.6342/NTU202501333

Contents

論文口試審定書 i

Acknowledgment ii

中文摘要 iii

Abstract iv

Table of Contents v

List of Figures viii

List of Tables xiv

1 Introduction 1

2 Features of Internal Waves 8

2.1 Radar Cross Section 10

2.2 Wind-Wave Model 15

doi:10.6342/NTU202501333

3 Implementation of XTI SAR Imaging **17**

3.1 Co-registration 18

3.2 Removal of Flat-Earth Phase 20

3.3 Multi-Satellite Constellation and Pair Averaging 21

3.4 Phase Unwrapping and Mean Filter 23

3.5 Elevation Mapping and Geometric Correction 25

3.6 Internal-Wave Signature Detection Constraints 27

3.6.1 Blind-Spot in SAR Images 28

3.6.2 Baseline Decorrelation and Center Frequency Shift 28

3.6.3 Trade-off between Horizontal Resolution and Vertical Accuracy . . . 30

4 Simulations and Discussion **32**

4.1 Velocity Bunching Effect 37

4.2 Effect of Baseline 43

4.3 Effect of Mean Filter Size 44

4.4 Selection of Baseline, Mean-Filter Size and Satellite Pair Number 46

4.5 Effect of Wind Speed 49

4.6 Detection of Subtle Internal-Wave Signatures 52

5 Conclusions **57**

doi:10.6342/NTU202501333

Bibliography **59**

Appendix: Registration Error Induced by Target Motion **71**

doi:10.6342/NTU202501333

List of Figures

2.1 Schematic of internal solitary wave moving in a two-layered ocean. 8

3.1 Geometry of single-pass XTI-SAR imaging with main and secondary platforms. 17

3.2 Flow-chart of XTI-SAR imaging algorithm. 19

3.3 Geometry of calculating flat-Earth phase. 20

3.4 Local coordinates referring to the nth satellite pair (P_{mn}, P_{sn}). 21

3.5 Grid points before (○) and after (●) interpolation. 22

3.6 Schematic of height estimation. 25

3.7 Schematic of geometric correction. 26

3.8 Contribution of internal wave in (2.26), simulated with parameters of event 1 in Table 4.1, (a) $\phi_{\text{iw}} = 0$, (b) $\phi_{\text{iw}} = \pi/2$. 28

3.9 Range spectral shift due to look-angle difference, $\Delta\theta \simeq -b_\perp/r_{0m}$, $b_\perp \ll H$. . 29

doi:10.6342/NTU202501333

4.1 Snapshots of sea-surface profile simulated with parameters of event 1 in Table 4.1, $U_{10} = 4$ m/s, and XTI-SAR images acquired with parameters listed in Table 4.2 and one satellite pair, (a) internal-wave signature immersed in wind wave, (b) reconstructed image of (a), RMSE = 15.38 cm, (c) internal-wave signature, (d) reconstructed image of (c), RMSE = 13.33 cm, (e) flat surface, (f) reconstructed image of (e), RMSE = 13.03 cm. 36

4.2 Simulated images with enhanced velocity bunching effect: (a) SAR image of sea-surface profile with internal-wave signature immersed in wind wave under $U_{10} = 4$ m/s, (b) SAR image of sea-surface profile with internal-wave signature, (c) XTI-SAR image of sea-surface profile with internal-wave signature immersed in wind wave under $U_{10} = 4$ m/s, RMSE = 16.28 cm, (d) XTI-SAR image of sea-surface profile with internal-wave signature, RMSE = 13.52 cm. 39

4.3 Height difference $\Delta\zeta$ between reconstructed profile and original profile, (a) $\Delta\zeta$ between Fig.4.1(b) and Fig.4.1(a), RMSE = 15.38 cm, (b) $\Delta\zeta$ between Fig.4.2(c) and Fig.4.1(a), RMSE = 16.28 cm, (c) $\Delta\zeta$ between Fig.4.1(f) and Fig.4.1(e), RMSE = 13.03 cm. 41

doi:10.6342/NTU202501333

4.4 Height difference $\triangle\zeta$ between reconstructed profile and original profile of internal-wave signature, (a) $\Delta\zeta$ between Fig.4.1(d) and Fig.4.1(c), RMSE = 13.34 cm, (b) $\Delta\zeta$ between Fig.4.2(d) and Fig.4.1(c), RMSE = 13.52 cm. . 42

4.5 XTI-SAR images of sea-surface profile simulated with parameters of event 1 in Table 4.1, U_{10} = 4 m/s, acquired with default parameters in Table 4.2 and different perpendicular baselines, (a) $b_\perp$ = 100 m, RMSE = 60.53 cm, RMSE_{iw} = 60.08 cm, (b) $b_\perp$ = 800 m, RMSE = 19.86 cm, RMSE_{iw} = 18.30 cm, (c) $b_\perp$ = 1500 m, RMSE = 15.69 cm, RMSE_{iw} = 13.75 cm, (d) $b_\perp$ = 3000 m, RMSE = 18.92 cm, RMSE_{iw} = 16.94 cm. 43

4.6 Effects of $b_\perp$ on (a) RMSE and (b) RMSE_{iw} of reconstructed images of Fig.4.1(a). 44

4.7 XTI-SAR images of a sea-surface profile acquired with default parameters in Table 4.2 and different mean-filter sizes, (a) $N_{wr} = 7$, $(w_x, w_y) = (14, 14)$ m, RMSE = 15.69 cm, RMSE_{iw} = 13.75 cm, (b) $N_{wr} = 37$, $(w_x, w_y) = (74, 74)$ m, RMSE = 9.79 cm, RMSE_{iw} = 3.98 cm, (c) $N_{wr} = 67$, $(w_x, w_y) = (134, 134)$ m, RMSE = 9.44 cm, RMSE_{iw} = 3.06 cm, (d) $N_{wr} = 97$, $(w_x, w_y) = (194, 194)$ m, RMSE = 9.32 cm, RMSE_{iw} = 2.69 cm. 45

4.8 Effects of mean-filter size on (a) RMSE and (b) RMSE_{iw} of reconstructed images of Fig.4.1(a). 46

doi:10.6342/NTU202501333

4.9 XTI-SAR images acquired from sea-surface profile of event 1 in Table 4.1, with default parameters in Table 4.2, U_{10} = 4 m/s, (a) simulated profile, (b) single pair, RMSE = 15.69 cm, RMSE_{iw} = 13.75 cm, (c) 5 pairs, RMSE = 9.80 cm, RMSE_{iw} = 6.40 cm, (d) 12 pairs, RMSE = 8.82 cm, RMSE_{iw} = 4.82 cm. 47

4.10 Effect of parameters on RMSE and RMSE_{iw} of sea-surface profiles simulated with parameters of event 1 in Table 4.1, $U_{10} = 4$ m/s, reconstructed with radar parameters listed in Table 4.2. Effect of (a) $b_\perp$ on RMSE, (b) $b_\perp$ on RMSE_{iw}, (c) w_x, w_y on RMSE, (d) w_x, w_y on RMSE_{iw}. ————: 1 pair, ————: 5 pairs, ————: 9 pairs, ————: 12 pairs. 48

4.11 XTI-SAR images acquired from sea-surface profile of event 1 in Table 4.1, with default parameters in Table 4.2, $U_{10} = 5$ m/s, (a) simulated profile, (b) single pair, $w_x = w_y = 14$ m, RMSE = 16.84 cm, RMSE_{iw} = 14.93 cm, (c) single pair, $w_x = w_y = 202$ m, $\text{RMSE}_{\text{iw}} = 2.94$ cm, (d) 12 pairs, $w_x = w_y = 50$ m, $\text{RMSE}_{\text{iw}} = 3.30$ cm. 49

doi:10.6342/NTU202501333

4.12 XTI-SAR images acquired from sea-surface profile of event 1 in Table 4.1, with default parameters in Table 4.2, $U_{10} = 6$ m/s, (a) simulated profile, (b) single pair, $w_x = w_y = 14$ m, RMSE = 18.29 cm, $\text{RMSE}_{\text{iw}} = 17.45$ cm, (c) single pair, $w_x = w_y = 202$ m, $\text{RMSE}_{\text{iw}} = 3.22$ cm, (d) 12 pairs, $w_x = w_y = 50$ m, $\text{RMSE}_{\text{iw}} = 4.98$ cm. 50

4.13 XTI-SAR images acquired from sea-surface profile of event 1 in Table 4.1, with default parameters in Table 4.2, $U_{10} = 9$ m/s, (a) simulated profile, (b) single pair, $w_x = w_y = 14$ m, RMSE = 26.89 cm, $\text{RMSE}_{\text{iw}} = 31.77$ cm, (c) single pair, $w_x = w_y = 202$ m, $\text{RMSE}_{\text{iw}} = 5.13$ cm, (d) 12 pairs, $w_x = w_y = 50$ m, $\text{RMSE}_{\text{iw}} = 22.37$ cm. 52

4.14 XTI-SAR images acquired from sea-surface profile of event 2 in Table 4.1, with default parameters in Table 4.2, $U_{10} = 3$ m/s, (a) simulated profile, (b) single pair, $w_x = w_y = 14$ m, RMSE = 13.79 cm, $\text{RMSE}_{\text{iw}} = 12.99$ cm, (c) single pair, $w_x = w_y = 202$ m, $\text{RMSE}_{\text{iw}} = 1.87$ cm, (d) 12 pairs, $w_x = w_y = 50$ m, $\text{RMSE}_{\text{iw}} = 1.32$ cm. 53

doi:10.6342/NTU202501333

4.15 XTI-SAR images acquired from sea-surface profile of event 2 in Table 4.1, carrying internal-wave signatures of alternate polarity, with default parameters in Table 4.2, $U_{10} = 3$ m/s, (a) simulated profile, (b) single pair, $w_x = w_y = 14$ m, RMSE = 13.96 cm, $\text{RMSE}_{\text{iw}} = 13.18$ cm, (c) single pair, $w_x = w_y = 202$ m, $\text{RMSE}_{\text{iw}} = 1.99$ cm, (d) 12 pairs, $w_x = w_y = 50$ m, $\text{RMSE}_{\text{iw}} = 1.30$ cm. . 54

4.16 XTI-SAR images of sea-surface profile acquired with default parameters in Table 4.2 and $N_{wr} = 97$, $(w_x, w_y) = (194, 194)$ m, (a) without enhancing velocity bunching effect, RMSE = 9.32 cm, (b) with enhanced velocity bunching effect, RMSE = 9.36 cm. 55

I.1 Schematic of slant range between satellite P and a moving target Q. 71

doi:10.6342/NTU202501333

List of Tables

4.1 Parameters of internal-wave event. 32

4.2 Parameters for reconstructing internal-wave signatures with multiple satellite pairs. 33

4.3 Azimuth angle ϕ_s of satellite pairs. 34

doi:10.6342/NTU202501333

Chapter 1

Introduction

A strong internal wave may endanger underwater activities and offshore rigs [1]. The water molecules dragged by an internal wave may plunge 240 m within 15 minutes [2], exerting a tremendous dragging force on submarines [3]. For example, the wreck site of an Indonesian Navy submarine was attributed to an internal wave with amplitude of about 40 m [4]. Early detection of an approaching internal wave is crucial to evade possible disasters.

A typical internal wave travels along the pycnocline, which is a layer of sea water featuring drastic density variation [1]. Various differential equations have been derived to model the propagation of internal wave under certain conditions of stratified water layers, including Kortweg-de Vries (KdV) equation [5], Gardner's equation [6], Benjamin-Ono equation [7], and so on. For example, the KdV equation implies a solitary waveform of squared hyperbolic secant function if the pycnocline thickness is infinitesimal [5].

An internal wave induces changes of sea-water properties, including temperature, salinity

doi:10.6342/NTU202501333

and density [2]. It also induces ocean current, arousing discernible surface signature [8] and surface solitary wave (SSW) [9], of which the amplitude and wavelength can be exploited to estimate the amplitude of the underlying internal wave [10]. Typical surface solitary waves have magnitude up to several decimeters [11], and wavelength of several hundred meters to several kilometers. Detecting such surface solitary waves requires images that can tell apart vertical difference in centimeters and horizontal resolution finer than tens of meters.

Internal wave can be detected with in-situ approaches or remote sensing techniques. In-situ approaches directly capture changes of physical properties induced by an internal wave [2]. However, such changes can only be detected at the deploying spots of the instruments, and the spatial scale of an internal wave cannot be acquired.

Remote sensing techniques have been used to detect sea-surface signatures of an internal wave, which may extend several kilometers along the crest [12]. For example, airborne infrared camera can capture change of sea-surface temperature, up to 0.5°, above an internal wave path, but its underlying mechanism remains on debate [13]. The change of sea surface profile above an internal wave can be captured by the naked eye [14] or using optical sensors [4], which are impeded by thick cloud or lack of daylight. The sea-surface height can also be acquired by using conventional altimeter that emits nadir pulses. However, its horizontal resolution of km is not sufficient for detecting internal wave [15].

doi:10.6342/NTU202501333

Synthetic aperture radar (SAR) can be used to detect internal waves by monitoring the variation of sea-surface roughness, without being constrained by clouds or daylight [8]. Information of an internal wave, including location, amplitude, traveling speed and water layers, can be extracted from the SAR images of the overlying sea surface [16]. For example, the traveling speed of an internal wave can be estimated by tracking the same signatures between two images taken apart by minutes to hours [17]. However, the internal-wave induced signatures on the sea surface is severely masked by wind waves at wind speed over 5 m/s [16]. In addition, an internal wave moves in parallel with the SAR platform cannot be manifested in the acquired SAR image.

By combining SAR imaging techniques to conventional altimetry, the along-track resolution of retrieved surface height information can be improved from km to hundreds of meters. In [11], dual-band SAR altimetry was carried out with Sentinel-3A to map the mean slope in an ocean area, which was combined with sea-level anomaly (SLA) to detect possible internal waves. A tandem configuration of Sentinel-6 for SAR imaging and Jason-3 for altimetry improved the horizontal resolution to hundreds of meters [18].

Interferometric SAR (InSAR) techniques [19] have been widely used to acquire digital elevation models (DEMs) [20], sea surface height (SSH) [21], glacial topography [22], glacier velocity [23], ocean current [24], and so on.

doi:10.6342/NTU202501333

In [8], an along-track interferometry (ATI) imaging experiment was conducted with TerraSAR-X to detect internal waves by measuring the Doppler velocity from the sea surface. The traveling speed of an internal wave is related to its induced sea-surface current [8], of which the speed and intensity can be estimated from the phase difference between the ATI radars [19].

Cross-track interferometric SAR (XTI-SAR) was used to build digital elevation model (DEM) [25]. The intrinsic range resolution of its constituent SAR imaging technique is better at incident angle near 30°, while typical InSAR altimetry adopts near-nadir incident angle [15]. In [26], an XTI-SAR at Ku-band with long baseline of about 1000 m was proposed to achieve the elevation accuracy of 1 cm and the horizontal resolution of 1 km.

Inherited from SAR altimetry, InSAR altimetry adopting near-nadir incidence could measure the elevation more accurately over a wide swath [15]. Examples of InSAR altimetry systems include Ku-band interferometric imaging radar altimeter (InIRA) on the Tiangong-2 space laboratory [27], Ka-band radar interferometer (KaRIn) on Surface Water and Ocean Topography (SWOT) [28] and Guanlan mission [21]. In [27], a Ku-band InIRA with short baseline (2.3 m) and small looking angle ($< 10°$) was carried out in the Tiangong-2 space laboratory to detect internal wave-induced sea-level anomaly, achieving elevation resolution of 20 cm and horizontal resolution of 40 m. In [28], a near-nadir Ka-band radar interferometer

doi:10.6342/NTU202501333

mounted on the SWOT satellite was used to map the ocean topography, leading to height accuracy of 10 cm and horizontal resolution of 50 m, or height accuracy of 1-2 cm and horizontal resolution of 1 km. In [29], a space-borne interferometric altimeter of a Guanlan mission was envisioned to achieve sea-surface height accuracy of centimeter and horizontal resolution of 0.5 km.

The working principles of InSAR altimetry and XTI-SAR are the same, with their major difference in the choice of look angle. They are both constrained by the trade-off between horizontal resolution and vertical accuracy, determined by the choice of look angle and mean filter width. As far as look angle is concerned, the vertical accuracy is better at near-nadir incidence, while the horizontal resolution is better at oblique incidence. The mean filter is widely applied in XTI-SAR imaging and InSAR altimetry to reduce random phase noise, thereby improving the vertical accuracy. By increasing the mean filter width, vertical accuracy is improved but horizontal resolution is compromised.

In this work, oblique incidence is adopted in XTI-SAR imaging to achieve fair horizontal resolution, while the elevation accuracy of internal-wave signatures is enhanced by collecting data from multiple satellite pairs to reduce noise before applying the phase unwrapping process. The caveat is the cost of deploying multiple satellite pairs, which is expected to significantly drop by leasing mega-constellation systems. Another noise reduction alternative

doi:10.6342/NTU202501333

is using nonlocal filter, which invokes high computational complexity and requires parameter tuning via machine-learning techniques [30],[31].

Multiple data sources have been exploited to retrieve internal wave information. In [32], internal wave was detected from satellite-borne SAR images, autonomous aerial vehicle (AAV) photographs, video recordings, and a variety of in-situ data. In [18], observation data from conventional altimeter were fused with SAR altimetry to enhance the elevation accuracy.

In [33], multiple Global Navigation Satellite System (GNSS) satellites were picked to form a multi-static repeat-pass InSAR system for acquiring 3D surface deformation. In [34], a bistatic differential InSAR (DInSAR) system, based on the GNSS satellite constellation, was proposed to concurrently acquire multiple images at different angles. In [35], squinted multi-satellite single-pass InSAR imaging was proposed by exploiting a pair of bistatic XTI-SAR satellites and a monostatic satellite to improve elevation accuracy.

In this work, multiple XTI-SAR satellite pairs are proposed to operate in monostatic mode at the altitudes of Starlink shells [36] to meet the stringent requirement on horizontal resolution and vertical accuracy for internal wave detection. The target area is illuminated by multiple satellite pairs from different directions, thereby mitigating the random phase noise. A two-step random phase cancellation process is performed, with an interpolation

doi:10.6342/NTU202501333

step to align the acquired images into the same grid, followed by a pair average process. A mean filter is applied after phase unwrapping process to further reduce phase error.

The rest of this thesis is organized as follows. The main features of internal waves are briefly reviewed in Chapter II, the proposed XTI-SAR imaging technique is presented in Chapter III, simulation results are discussed in Chapter IV, followed by some conclusions in Chapter V.

doi:10.6342/NTU202501333

Chapter 2

Features of Internal Waves

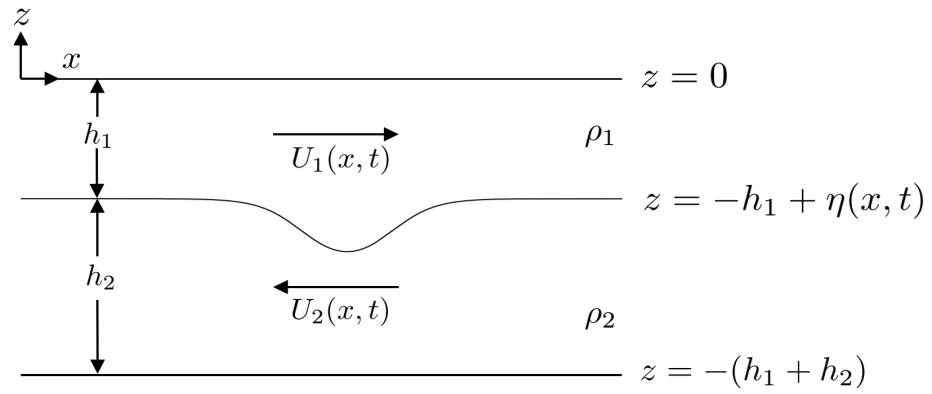

Figure 2.1: Schematic of internal solitary wave moving in a two-layered ocean.

A typical ocean is stratified into three layers: a mixed layer where sea-water density is nearly constant, a pycnocline with large density gradient, and a deep layer where sea-water density becomes nearly constant again [37]. When the depth of pycnocline is perturbed, for example, by change of underwater topography [38], the displacement of pycnocline depth will propagate as an internal wave.

In practice, the pycnocline is approximated as infinitesimally thin, forming a two-layered ocean. Fig.2.1 shows the schematic of an internal solitary wave moving in a two-layered

doi:10.6342/NTU202501333

ocean, where h_1 and h_2 are the thicknesses of upper and lower layers, respectively. U_1 and U_2 are ocean current velocities in the upper and lower layers, respectively, $\eta(x,t)$ is the pycnocline displacement associated with the internal solitary wave, which satisfies the continuity equation [8], leading to

$$U_1(x,t) = -\frac{c_{\rm iw}\eta(x,t)}{h_1 - \eta(x,t)} \tag{2.1}$$

where $c_{\rm iw}$ is the phase speed of the internal solitary wave.

Without loss of generality, assume the pycnocline displacement $\eta(x,t)$ moves in x direction, satisfying the KdV equation [16]

$$\frac{\partial\eta}{\partial t} + c_{\rm iw0}\frac{\partial\eta}{\partial x} + \alpha\eta\frac{\partial\eta}{\partial x} + \beta\frac{\partial^3\eta}{\partial x^3} = 0 \tag{2.2}$$

where $\alpha = 3c_{\rm iw0}(h_1 - h_2)/(2h_1h_2)$, $\beta = c_{\rm iw0}h_1h_2/6$, $c_{\rm iw0} = \sqrt{g\Delta\rho h_1h_2/[\rho(h_1+h_2)]}$ is the linear phase velocity of the internal wave, g is the gravitational acceleration, $\Delta\rho = \rho_2 - \rho_1$ is the density difference between the two layers. The average density can be approximated as $\rho \simeq (\rho_1+\rho_2)/2$ if $\Delta\rho \ll \rho_1, \rho_2$.

A solution of (2.2) is given by [39]

$$\eta(x,t) = \eta_0 \mathrm{sech}^2\left(\frac{x - c_{\rm iw}t}{\ell}\right) \tag{2.3}$$

where ℓ is the half-width of solitary wave [16]. The wave amplitude is

$$\eta_0 = \frac{4h_1^2h_2^2}{3\ell^2(h_1 - h_2)} \tag{2.4}$$

doi:10.6342/NTU202501333

and the phase velocity is [16]

$$c_{\text{iw}} = c_{\text{iw0}} \left[1 + \frac{\eta_0 (h_1 - h_2)}{2 h_1 h_2} \right] \tag{2.5}$$

Eqn.(2.3) is mapped to a two-dimensional wave as

$$\eta(x, y, t) = \eta_0 \text{sech}^2 \left(\frac{x \cos \phi_{\text{iw}} + y \sin \phi_{\text{iw}} - c_{\text{iw}} t}{\ell} \right) \tag{2.6}$$

where ϕ_{iw} is the azimuthal direction of propagation with respect to the x axis.

The sea-surface displacement $\zeta(x, t)$, aroused by an internal wave displacement $\eta(x, t)$, is approximated as another solitary wave moving at the same speed with that of $\eta(x, t)$ [10]. The ratio of these two displacements is given by [10], [40], [41]

$$\frac{\zeta_{\text{iw}}(x, t)}{\eta(x, t)} = -\frac{c_{\text{iw0}}^2}{c_{\text{iw0}}^2 - g h_1} \simeq \frac{-h_2}{h_1 + h_2} \delta \tag{2.7}$$

if $\delta = \Delta\rho / \rho \ll 1$. By substituting (2.3) into (2.7), we have

$$\zeta_{\text{iw}}(x, t) \simeq \frac{-h_2 \delta}{h_1 + h_2} \eta_0 \text{sech}^2 \left(\frac{x - c_{\text{iw}} t}{\ell} \right) \tag{2.8}$$

which is mapped to a two-dimensional wave as

$$\zeta_{\text{iw}}(x, y, t) \simeq \frac{-h_2 \delta}{h_1 + h_2} \eta_0 \text{sech}^2 \left(\frac{x \cos \phi_{\text{iw}} + y \sin \phi_{\text{iw}} - c_{\text{iw}} t}{\ell} \right) \tag{2.9}$$

2.1 Radar Cross Section

An internal wave can be detected by means of the normalized radar cross section (NRCS) from its induced surface displacement. The Bragg scattering dominates at moderate incident

doi:10.6342/NTU202501333

angles of 20-70° [42], satisfying the condition

$$2\lambda_w \sin\theta_i = n\lambda_0 \text{ or } k_w = \frac{2k_0 \sin\theta_i}{n} \tag{2.10}$$

where n is an integer, θ_i is the incident angle, λ_0 (k_0) is the incident wavelength (wavenumber), and λ_w (k_w) is the sea-surface wavelength (wavenumber) of interest.

For an ocean current moving at speed $\bar{U}(\bar{r},t)$, its apparent angular frequency $\omega(\bar{k},\bar{r},t)$ is related to its intrinsic angular frequency $\omega_0(\bar{k})$ and the wavenumber vector $\bar{k}$ as [43]

$$\omega(\bar{k},\bar{r},t) = \omega_0(\bar{k}) + \bar{k}(\bar{r},t)\cdot\bar{U}(\bar{r},t) \tag{2.11}$$

where $\omega_0(\bar{k})$ satisfies the dispersion relation [43]

$$\omega_0(\bar{k}) = \sqrt{gk + \gamma k^3} \tag{2.12}$$

$k = |\bar{k}|$, $\gamma = \tau_s/\rho_1$, τ_s and ρ_1 are surface tension and water mass density, respectively.

A wave-action spectral density is defined as [43]

$$N(\bar{k}) = \frac{E(\bar{k})}{\omega_0(\bar{k})} = \frac{\rho_1(g+\gamma k^2)\Psi(\bar{k})}{\omega_0(\bar{k})} \simeq \frac{\rho_1 g\Psi(\bar{k})}{\omega_0(\bar{k})} \tag{2.13}$$

where $E(\bar{k})$ (kg-m^2/s^2) is the energy spectral density and $\Psi(\bar{k})$ (m^4) is wave-height spectral density.

When a wave packet of very narrow band propagates in an ocean current which moves at speed $\bar{U}(\bar{r},t)$, the wave action deviates from its equilibrium state $N_{\text{eq}}(\bar{k})$ and satisfies an

doi:10.6342/NTU202501333

action balance equation [43], [44]

$$\left(\frac{\partial}{\partial t}+\frac{d\bar{r}}{dt}\frac{\partial}{\partial \bar{r}}+\frac{d\bar{k}}{dt}\frac{\partial}{\partial \bar{k}}\right)N(\bar{k},\bar{r},t)=Q_n(\bar{k},\bar{r},t) \tag{2.14}$$

where $Q_n(\bar{k},\bar{r},t)$ is the source function. By the definition in (2.13), (2.14) is reduced to a balance equation of wavenumber spectrum [16]

$$\frac{\partial \Psi(\bar{k},\bar{r},t)}{\partial t}+[\bar{c}_g(\bar{k})+\bar{U}(\bar{r},t)]\cdot\nabla\Psi(\bar{k},\bar{r},t)=Q(\bar{k},\bar{r},t) \tag{2.15}$$

with the source function

$$Q(\bar{k},\bar{r},t)=S_{\text{in}}(\bar{k})+S_{\text{n}\ell}(\bar{k})+S_{\text{ds}}(\bar{k})+S_{\text{cu}}(\bar{k},\bar{r},t) \tag{2.16}$$

where

$$S_{\text{in}}(\bar{k})=m\left(\frac{u_*}{c_{\text{s0}}}\right)^2\omega_0\left|\cos(\phi-\phi_w)\right|\Psi(\bar{k}) \tag{2.17}$$

is the wind-driven source function, $m=0.04$, u_* is the wind friction velocity at sea-surface, $c_{\text{s0}}=\omega_0/k$, ϕ_w is the wind direction about the x axis, and $\phi=\tan^{-1}(k_y/k_x)$, with $\bar{k}=k_x\hat{x}+k_y\hat{y}$;

$$S_{\text{n}\ell}(\bar{k})=-m_3\omega_0k^{-4}B^2(\bar{k})=-m_3\omega_0k^4\Psi^2(\bar{k}) \tag{2.18}$$

is the nonlinear wave-wave interaction source function in gravity-capillary band [16], $m_3=0.13$ [39], and $B(\bar{k})=k^4\Psi(\bar{k})$;

$$S_{\text{ds}}(\bar{k})=-4\nu k^2\Psi(\bar{k}) \tag{2.19}$$

doi:10.6342/NTU202501333

is the dissipation source function due to viscosity, ν is the kinematic viscosity; and

$$S_{\mathrm{cu}}(\bar{k},\bar{r},t) = -S_{\alpha\beta}\frac{\partial U_\beta}{\partial x_\alpha}\Psi(\bar{k}) \tag{2.20}$$

is the wave-current interaction source function, U_β is the β component of the ocean surface current velocity [16], $S_{\alpha\beta}\partial U_\beta/\partial x_\alpha$ is the excess momentum flux tensor at high frequencies.

If the wind blows steadily over the ocean surface, the wave-action spectral density $N(\bar{k})$ and the wave-height spectral density $\Psi(\bar{k})$ are independent of time. Both the time derivative and the gradient of $\Psi(\bar{k})$ vanish, which means the advection of short waves in short gravity, gravity-capillary and capillary bands are neglected in equilibrium [16], namely,

$$\frac{\partial\Psi(\bar{k})}{\partial t} = 0, \quad \nabla\Psi(\bar{k}) = 0$$

Then, (2.15) implies

$$Q = 0 \tag{2.21}$$

or

$$m\left(\frac{u_*}{c_{\mathrm{s0}}}\right)^2\omega_0\left|\cos(\phi-\phi_w)\right|\Psi(\bar{k}) - m_3\omega_0 k^4\Psi^2(\bar{k}) - 4\nu k^2\Psi(\bar{k}) - S_{\alpha\beta}\frac{\partial U_\beta}{\partial x_\alpha}\Psi(\bar{k}) = 0 \tag{2.22}$$

which is solved to obtain the wave-height spectral density [16]

$$\Psi(k,\phi) = m_3^{-1}k^{-4}\left[m\left(\frac{u_*}{c_{\mathrm{s0}}}\right)^2\left|\cos(\phi-\phi_w)\right| - 4\nu k^2\omega_0^{-1} - S_{\alpha\beta}\frac{\partial U_\beta}{\partial x_\alpha}\omega_0^{-1}\right] \tag{2.23}$$

doi:10.6342/NTU202501333

where the third term on the right-hand side is relabeled as $\Delta\Psi(\bar{k})$, which is the modulation on the ocean surface current by an underwater internal wave. Explicitly,

$$\Delta\Psi(k,\phi) = -\frac{1}{2} m_3^{-1} k^{-4} \omega_0^{-1} \cos(\phi - \phi_{\rm iw}) \left[\cos\phi \frac{\partial U_1(x,y,t)}{\partial x} + \sin\phi \frac{\partial U_1(x,y,t)}{\partial y} \right] \quad (2.24)$$

By using (2.1) and (2.6), under the approximation of $\eta(x,t) \ll h_1$, (2.24) is reduced to

$$\begin{aligned} \Delta\Psi(k,\phi) \simeq & -m_3^{-1} k^{-4} \ell^{-1} \eta_0 \omega_0^{-1} \frac{c_{\rm iw}}{h_1} \cos^2(\phi - \phi_{\rm iw}) \\ & \operatorname{sech}^2 \left(\frac{x\cos\phi_{\rm iw} + y\sin\phi_{\rm iw} - c_{\rm iw} t}{\ell} \right) \tanh \left(\frac{x\cos\phi_{\rm iw} + y\sin\phi_{\rm iw} - c_{\rm iw} t}{\ell} \right) \end{aligned} \quad (2.25)$$

Next, substitute (2.25) into (2.23) to have the wave-height spectral density $\Psi(k,\phi)$. The normalized radar cross section (NRCS) of backscattering at incident angle θ_i is given by [16], [45]

$$\begin{aligned} \sigma_0^{ab}(\theta_i) = 16\pi k_0^4 |g_{ab}(\theta_i)|^2 \Psi(k_w, 0) = 16\pi k_0^4 |g_{ab}(\theta_i)|^2 m_3^{-1} k_w^{-4} \Bigg[m \left(\frac{u_*}{c_{\rm s0}} \right)^2 |\cos\phi_w| - 4\nu k_w^2 \omega_0^{-1} \\ - \frac{\eta_0 c_{\rm iw} \cos^2\phi_{\rm iw}}{\omega_0 h_1 \ell} \operatorname{sech}^2 \left(\frac{x\cos\phi_{\rm iw} + y\sin\phi_{\rm iw} - c_{\rm iw} t}{\ell} \right) \\ \tanh \left(\frac{x\cos\phi_{\rm iw} + y\sin\phi_{\rm iw} - c_{\rm iw} t}{\ell} \right) \Bigg] \end{aligned} \quad (2.26)$$

where k_w is determined by imposing (2.10), $a = h, v$ is the transmitting polarization, and $b = h, v$ is the receiving polarization. The first-order scattering coefficient at hh-pol is given by

$$g_{hh}(\theta_i) = \frac{(\epsilon_r - 1)\cos^2\theta_i}{\left(\cos\theta_i + \sqrt{\epsilon_r - \sin^2\theta_i} \right)^2}$$

doi:10.6342/NTU202501333

and that at vv-pol is given by

$$g_{vv}(\theta_i) = \frac{(\epsilon_r - 1)[\epsilon_r(1 + \sin^2\theta_i) - \sin^2\theta_i]\cos^2\theta_i}{\left(\epsilon_r \cos\theta_i + \sqrt{\epsilon_r - \sin^2\theta_i}\right)^2}$$

where ϵ_r is the relative dielectric constant of sea water, given by a double Debye dielectric model (D3M) [39]. Eqn.(2.26) indicates that $\sigma_0^{ab}(\theta_i) = 0$ at $\phi_{\rm iw} = \pi/2$, when an internal wave moves perpendicularly to the radar beam direction.

2.2 Wind-Wave Model

Typical two-dimensional wind-wave spectrum $\Psi(k_x, k_y)$ can be represented as an omnidirectional spectrum $S(k)$ multiplied by an angular spread function $\Phi(k, \phi)$ as

$$\Psi(k_x, k_y) = \frac{1}{k} S(k)\Phi(k, \phi) \tag{2.27}$$

where $k_x = k\cos\phi$ and $k_y = k\sin\phi$. In the Pierson-Moscowitz model, the omnidirectional spectrum is given by [46]

$$S_{\rm pm}(k) = \frac{\alpha}{2k^3} \exp\left\{-\beta\left(\frac{g}{k}\right)^2 \frac{1}{U_{19}^4}\right\} \tag{2.28}$$

where $\alpha = 0.0081$, $\beta = 0.74$, U_{19} is the wind speed at 19.5 m above the ocean surface, which is related to U_{10} as [46]

$$U_{19} \simeq 1.026 U_{10} \tag{2.29}$$

doi:10.6342/NTU202501333

The dispersion relation of $\omega = \sqrt{gk}$ is imposed, which holds for $k \ll \sqrt{g/\gamma_s} \simeq 363.2$ rad/m. Eqn.(2.28) applies to fully-developed seas where steady wind blows for an infinitely long time over an infinitely long fetch.

The angular spread function $\Phi(k, \phi)$ is normalized such that

$$\int_0^{2\pi} \Phi(k, \phi) d\phi = 1 \tag{2.30}$$

A cosine-2s spreading function is given by [47]

$$\Phi_c(k, \phi) = G(s) \left| \cos\left(\frac{\phi - \phi_0}{2}\right) \right|^{2s} \tag{2.31}$$

with

$$\begin{aligned} s &= 11.5 \left[\frac{c_{\mathrm{s}0}(k)}{U_{10}}\right]^{2.5} \\ G(s) &= \frac{1}{2\sqrt{\pi}} \frac{\Gamma(s+1)}{\Gamma(s+0.5)} \end{aligned} \tag{2.32}$$

where $c_{\mathrm{s}0} = \omega_0(k)/k$, $\Gamma(x)$ is the gamma function, and $G(s)$ can be approximated as

$$G(s) \simeq \frac{\sqrt{s}}{2\sqrt{\pi}}$$

under large s.

The sea-surface profile $\zeta(x, y, t)$ used in the simulation is given by

$$\zeta(x, y, t) = \zeta_{\mathrm{iw}}(x, y, t) + \zeta_{\mathrm{u}10}(x, y, t) \tag{2.33}$$

where $\zeta_{\mathrm{u}10}(x, y, t)$ is the wind-wave simulated with (2.28).

doi:10.6342/NTU202501333

Chapter 3

Implementation of XTI SAR Imaging

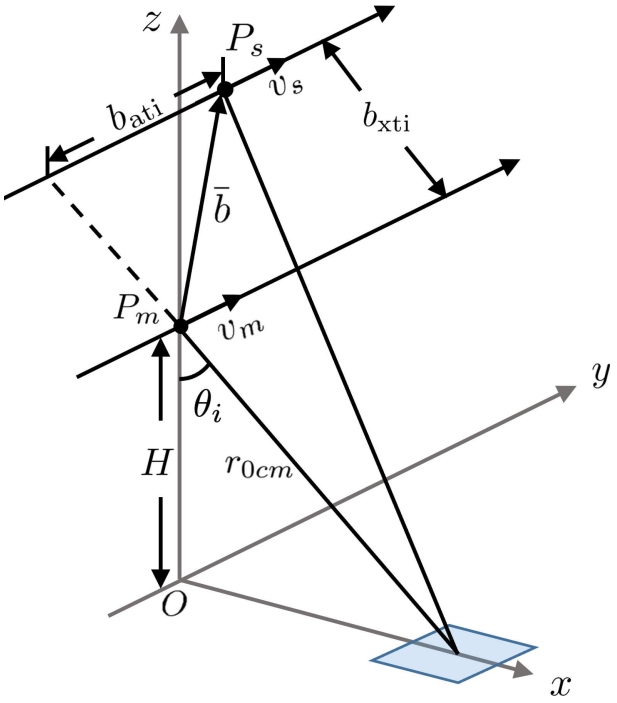

Figure 3.1: Geometry of single-pass XTI-SAR imaging with main and secondary platforms.

Fig.3.1 shows the geometry of a single-pass XTI-SAR imaging, with main platform (P_m) and secondary platform (P_s) moving in parallel along track [19]. The origin is set to the nadir point of the main platform at $\eta = 0$, The main platform has a constant altitude H and moves in the y direction, the z direction points upwards, the squint angle is set zero without

doi:10.6342/NTU202501333

loss of generality.

The main platform and the secondary platform are separated by a baseline vector $\overline{b} = [b_x, b_y, b_z]^t$, the cross-track baseline is $b_{\text{xti}} = \sqrt{b_x^2 + b_z^2}$, and the along-track baseline is $b_{\text{ati}} = b_y$, which is set to zero without loss of generality.

The incident angle measured from the main platform is θ_i. The ocean surface profile is given by $z = \zeta(x, y)$, with the mean sea level at $z = 0$, which is approximated as a connected set of tilted facets in computing the backscattered radar signals.

The closest range from the main platform to the n_rth range cell is given by $r_{0m}[n_r] = c\tau[n_r]/2$, with $\tau[n_r] = 2r_{0cm}/c + (n_r - 1 - N_r/2)\Delta\tau$, $r_{0cm} = r_{0m}[N_r/2 + 1] = H/\cos\theta_i$ is the closest range between the main platform and the swath center, and the corresponding fast time is $\tau_0 = 2r_{0cm}/c$.

Fig.3.2 shows the flow-chart of XTI-SAR imaging algorithm for acquiring the sea surface profile [20].

3.1 Co-registration

Denote the main image as $s_m[n_r, n_a]$ and the secondary image as $s_s[n_r, n_a]$, with $n_r = 1, 2, \cdots, N_r$ and $n_a = 1, 2, \cdots, N_a$. Conduct a coarse co-registration process on the secondary image to have

$$s_{s1}[n_r, n_a] = s_s[n_r + \Delta n_r, n_a + \Delta n_a] \tag{3.1}$$

doi:10.6342/NTU202501333

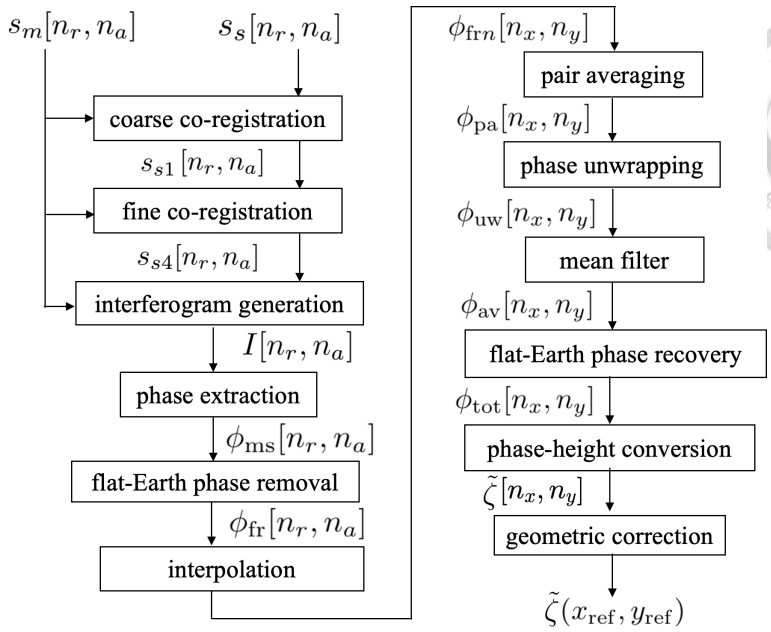

Figure 3.2: Flow-chart of XTI-SAR imaging algorithm.

where Δn_r and Δn_a are integers determined by maximizing a correlation function between $s_m[n_r, n_a]$ and $s_s[n_r, n_a]$ [31].

A fine co-registration process is conducted by first oversampling the secondary image $s_{s1}[n_r, n_a]$ by a factor N_s in range direction [48]. Then, divide the secondary image into $N_{rt} \times N_{at}$ sub-images, with $N_{rp} \times N_{ap}$ pixels in each sub-image.

Similarly, the main image is divided into $N_{rt} \times N_{at}$ sub-images. The optimal fine shifts are estimated by maximizing the correlation function between each pair of main sub-image and secondary sub-image. Finally, the co-registered secondary sub-images are concatenated to form the co-registered secondary image $s_{s4}[n_r, n_a]$.

doi:10.6342/NTU202501333

3.2 Removal of Flat-Earth Phase

The interferogram is computed as

$$I[n_r, n_a] = s_m[n_r, n_a] s_{s4}^*[n_r, n_a] \tag{3.2}$$

and the interferometric phase is extracted as

$$\phi_{\text{ms}}[n_r, n_a] = \arg\{I[n_r, n_a]\} \tag{3.3}$$

which is dominated by the flat-Earth phase.

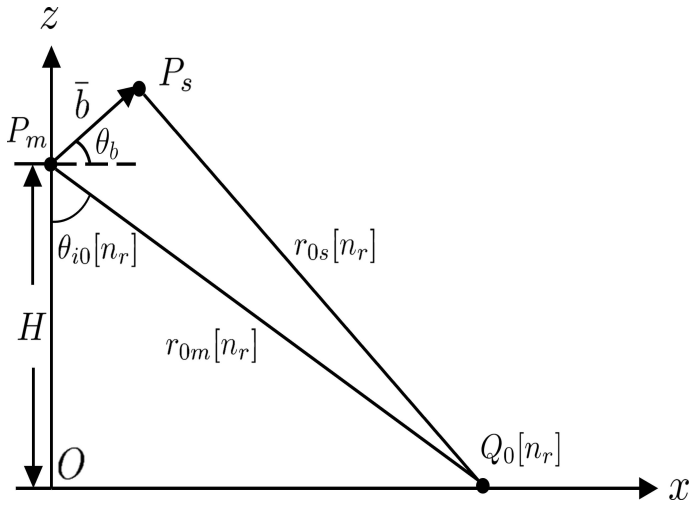

Figure 3.3: Geometry of calculating flat-Earth phase.

Fig.3.3 shows the geometry of calculating the flat-Earth phase. By the law of cosines, the closest range between the secondary platform to the n_rth range cell is

$$r_{0s}[n_r] = \left[(r_{0m}[n_r])^2 + b^2 - 2b r_{0m}[n_r] \cos\left(\frac{\pi}{2} - \theta_{i0}[n_r] + \theta_b \right) \right]^{1/2}$$

where $b = |\bar{b}|$, $\theta_b = \cos^{-1}(b_x/b)$, and $\theta_{i0}[n_r] = \cos^{-1}(H/r_{0m}[n_r])$ is the local incident angle.

doi:10.6342/NTU202501333

The flat-Earth phase is

$$\phi_{\text{fe}}[n_r] = -(4\pi/\lambda)(r_{0m}[n_r] - r_{0s}[n_r]) \tag{3.4}$$

which is removed from (3.3) to have

$$\phi_{\text{fr}}[n_r, n_a] = \phi_{ms}[n_r, n_a] - \phi_{fe}[n_r] \tag{3.5}$$

3.3 Multi-Satellite Constellation and Pair Averaging

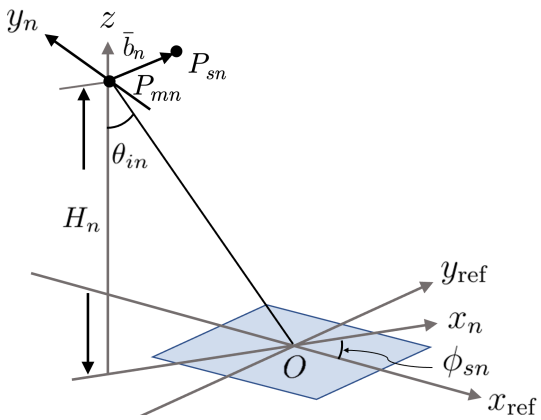

Figure 3.4: Local coordinates referring to the nth satellite pair (P_{mn}, P_{sn}).

Fig.3.4 shows the local coordinates (x_n, y_n, z) referring to the nth satellite pair. A main satellite P_{mn} flies in the y_n direction at a constant altitude H_n, and a secondary satellite P_{sn} flies in parallel with P_{mn}, separated by a baseline vector $\bar{b}_n$ from the former. The global coordinates $(x_{\text{ref}}, y_{\text{ref}}, z)$ apply to all the satellite pairs, with an angle ϕ_{sn} between x_n and x_{ref} axes. The unit vectors in these two coordinate systems are related as

$$\hat{x}_n = \hat{x}_{\text{ref}} \cos\phi_{sn} + \hat{y}_{\text{ref}} \sin\phi_{sn}$$

doi:10.6342/NTU202501333

$$\hat{y}_n = -\hat{x}_{\text{ref}} \sin\phi_{sn} + \hat{y}_{\text{ref}} \cos\phi_{sn}$$

Fig.3.5 shows a target area of size $L_x \times L_y$, which is divided into a uniform grid of spacings $\Delta x = L_x/N_x$ and $\Delta y = L_y/N_y$. The horizontal position of pixel $[n_x, n_y]$ in the global coordinates is specified as $\bar{r}[n_x, n_y] = \hat{x}_{\text{ref}} x_{\text{ref}}[n_x, n_y] + \hat{y}_{\text{ref}} y_{\text{ref}}[n_x, n_y]$, with

$$x_{\text{ref}}[n_x, n_y] = n_x \Delta x, \;\; y_{\text{ref}}[n_x, n_y] = n_y \Delta y \tag{3.6}$$

where $-N_x/2 \le n_x \le N_x/2 - 1$ and $-N_y/2 \le n_y \le N_y/2 - 1$. The horizontal position of pixel $[n_r, n_a]$ in the local coordinates is specified as $\bar{r}[n_r, n_a] = \hat{x}_n x_n[n_r, n_a] + \hat{y}_n y_n[n_r, n_a]$, with

$$x_n[n_r, n_a] = \sqrt{(c\tau[n_r]/2)^2 - H_n^2}$$

$$y_n[n_r, n_a] = v_s \eta[n_a] \tag{3.7}$$

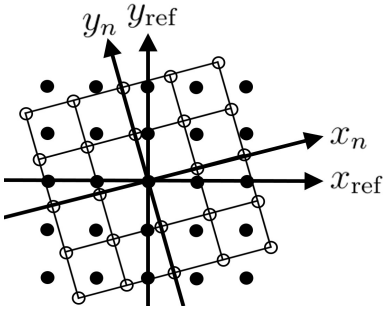

Figure 3.5: Grid points before (○) and after (●) interpolation.

The horizontal position $(x_{\text{ref}}, y_{\text{ref}})$ is mapped to (x_n, y_n) as

$$x_n[n_x, n_y] = x_{\text{ref}}[n_x, n_y] \cos\phi_{sn} + y_{\text{ref}}[n_x, n_y] \sin\phi_{sn}$$

$$y_n[n_x, n_y] = -x_{\text{ref}}[n_x, n_y] \sin\phi_{sn} + y_{\text{ref}}[n_x, n_y] \cos\phi_{sn}$$

doi:10.6342/NTU202501333

The phase derived from the nth satellite pair is removed off the flat-Earth phase, then interpolated to the global coordinates via (3.7) as $\phi_{\text{frn}}[n_x, n_y]$. The final phase is estimated by averaging the interpolated phases over N satellite pairs, namely,

$$\phi_{\text{pa}}[n_x, n_y] = \arg\left\{\sum_{n=1}^{N} e^{j\phi_{\text{frn}}[n_x, n_y]}\right\} \tag{3.8}$$

3.4 Phase Unwrapping and Mean Filter

The first phase of noise mitigation is performed by pair averaging, so that (3.8) is ready for phase unwrapping. The unwrapped phase $\phi'_{\text{un}}[n_x, n_y]$ is related to $\phi_{\text{pa}}[n_x, n_y]$ as [49]

$$\phi'_{\text{un}}[n_x, n_y] = \phi_{\text{pa}}[n_x, n_y] + 2\pi\Lambda[n_x, n_y]$$

where $\Lambda[n_x, n_y]$ is an integer. If the Nyquist criterion is met, the phase difference between adjacent pixels is always less than π (rad.) [20]. A wrapping operator is defined as

$$W(\phi) = \phi - 2\pi \left\lfloor \frac{\phi + \pi}{2\pi} \right\rfloor$$

which wraps phase ϕ into the interval $(-\pi, \pi]$ [50].

Define an error of phase $\phi_{\text{pa}}[n_x + 1, n_y + 1]$ to its linear approximation $\hat{\phi}_{\text{pa}}[n_x + 1, n_y + 1]$ as [50]

$$t[n_x, n_y] = \left| W(\hat{\phi}_{\text{pa}}[n_x + 1, n_y + 1] - \phi_{\text{pa}}[n_x + 1, n_y + 1]) \right|$$

doi:10.6342/NTU202501333

with smaller $t[n_x, n_y]$ implying higher reliability. Then, define a quality function as [51]

$$Q[n_x, n_y] = 1 - \frac{t[n_x, n_y]}{\pi} \tag{3.9}$$

which falls in $[0, 1]$, with larger value implying better quality.

A quality-guided phase unwrapping algorithm is applied along a path which is immune to error propagation, based on the quality function defined in (3.9) [52]. The pixel with the highest quality in the whole image is selected as the starting point and its four neighbors are stored in an adjoin list. Next, select the pixel p with the highest quality from the adjoin list, its unwrapped phase is computed as

$$\phi_w + 2\pi \left\lfloor \frac{\phi_r - \phi_w + \pi}{2\pi} \right\rfloor$$

where ϕ_w is its wrapped phase and ϕ_r is the phase of a reference pixel which is arbitrarily picked from an unwrapped neighboring pixel of p.

Pixel p is then removed from the adjoin list, and its neighboring pixels which have not been unwrapped are added to the list. The procedure continues until the list is empty. The unwrapped interferometric phase is labeled as $\phi'_{un}[n_x, n_y]$.

To further reduce noises, a mean filter with size $N_{wr} \times N_{wa}$, is applied to $\phi'_{un}[n_x, n_y]$ to obtain [20]

$$\phi_{\text{av}}[n_x, n_y] = \arg \left\{ \sum_{n=-(N_{wa}-1)/2}^{(N_{wa}-1)/2} \sum_{m=-(N_{wr}-1)/2}^{(N_{wr}-1)/2} e^{j\phi_{\text{un}}[n_x+m, n_y+n]} \right\}$$

doi:10.6342/NTU202501333

3.5 Elevation Mapping and Geometric Correction

Next, the flat-Earth phase in (3.4) is modified from $[n_r, n_a]$ to $[n_x, n_y]$ by noting

$$r_{0m}[n_x] = \sqrt{H^2 + (H\tan\theta_{i0} + n_x\Delta x)^2}$$

$$r_{0s}[n_x] = \left[(r_{0m}[n_x])^2 + b^2 \ -2br_{0m}[n_x]\cos\left(\frac{\pi}{2} - \theta_{i0}[n_x] + \theta_b\right)\right]^{1/2} \tag{3.10}$$

where $b = |\bar{b}|$, $\theta_b = \cos^{-1}(b_x/b)$, and $\theta_{i0}[n_x] = \cos^{-1}(H/r_{0m}[n_x])$ is the local incident angle. The modified flat-Earth phase is

$$\phi'_{\text{fe}}[n_x] = -(4\pi/\lambda)(r_{0m}[n_x] - r_{0s}[n_y]) \tag{3.11}$$

and is added back to the mean-filtered phase as

$$\phi_{\text{tot}}[n_x, n_y] = \phi_{\text{av}}[n_x, n_y] + \phi'_{\text{fe}}[n_x] \tag{3.12}$$

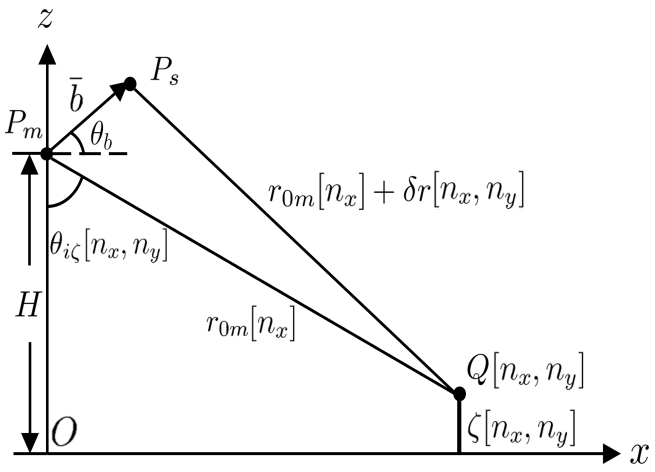

Figure 3.6: Schematic of height estimation.

Fig.3.6 shows that the estimated elevation at pixel $[n_x, n_y]$ is related to the range from

doi:10.6342/NTU202501333

the main platform as

$$\tilde{\zeta}[n_x, n_y] = H - r_{0m}[n_x] \cos\theta_{i\zeta}[n_x, n_y] \tag{3.13}$$

where the range difference $\delta r[n_x, n_y]$ is related to $\phi_{\text{tot}}[n_x, n_y]$ as

$$\phi_{\text{tot}}[n_x, n_y] \simeq \frac{4\pi\delta r[n_x, n_y]}{\lambda} \tag{3.14}$$

By the law of cosines that

$$(r_{0m}[n_x] + \delta r[n_x, n_x])^2 = r_{0m}^2[n_x] + b^2 - 2br_{0m}[n_x] \cos\left(\theta_b + \frac{\pi}{2} - \theta_{i\zeta}[n_x, n_y]\right) \tag{3.15}$$

we have

$$\theta_{i\zeta}[n_x, n_y] \simeq \theta_b - \frac{\pi}{2} + \cos^{-1}\frac{\delta r[n_x, n_y]}{b} \tag{3.16}$$

under the assumption that $r_{0m} \gg \delta r$ and $r_{0m} \gg b$. The elevation $\zeta[n_x, n_y]$ is then estimated by substituting (3.14) into (3.16), then into (3.13).

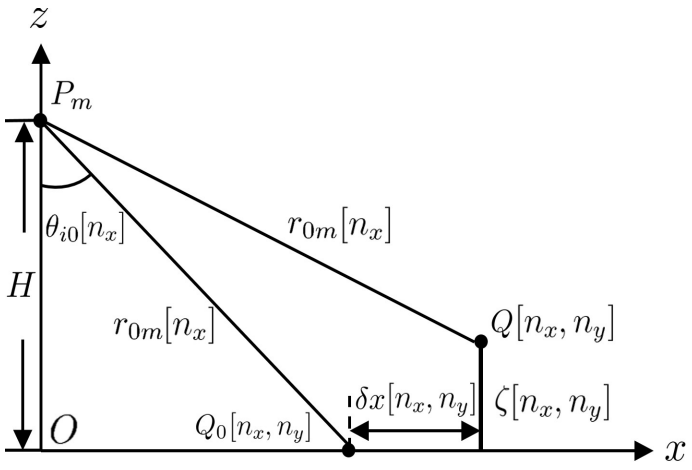

Figure 3.7: Schematic of geometric correction.

doi:10.6342/NTU202501333

As three-dimensional topographic surface is mapped to two-dimensional InSAR image, the horizontal position of a point on the surface is deviated on the image. Geometric correction is required to map the InSAR image of surface elevation, $\zeta[n_x, n_y]$, from $[n_x, n_y]$ to correct position (x, y). Fig.3.7 shows the schematic of geometric correction. The point $Q[n_r, n_a]$ is mapped to $Q_0[n_r, n_a]$, which is shifted by $\delta x[n_r, n_a]$ and satisfies $\overline{P_m Q_0} = \overline{P_m Q}$, namely,

$$(H \tan\theta_{i0} + \delta x)^2 + (H - \zeta)^2 = r_{0m}^2$$

from which δx is solved as

$$\delta x \simeq \zeta \cot\theta_{i0} \tag{3.17}$$

Thus, the horizontal position of the XTI-SAR surface elevation $\zeta[n_r, n_a]$ at pixel $[n_x, n_y]$ is corrected as

$$x = \delta x[n_r, n_a] + x_{\text{ref}}$$

$$y = y_{\text{ref}}$$

3.6 Internal-Wave Signature Detection Constraints

In the rest of this Chapter, three constraints on applying the proposed method for detecting internal-wave signature are elaborated, including blind-spot in SAR images, baseline

doi:10.6342/NTU202501333

decorrelation and center frequency shift, trade-off between horizontal resolution and vertical accuracy.

3.6.1 Blind-Spot in SAR Images

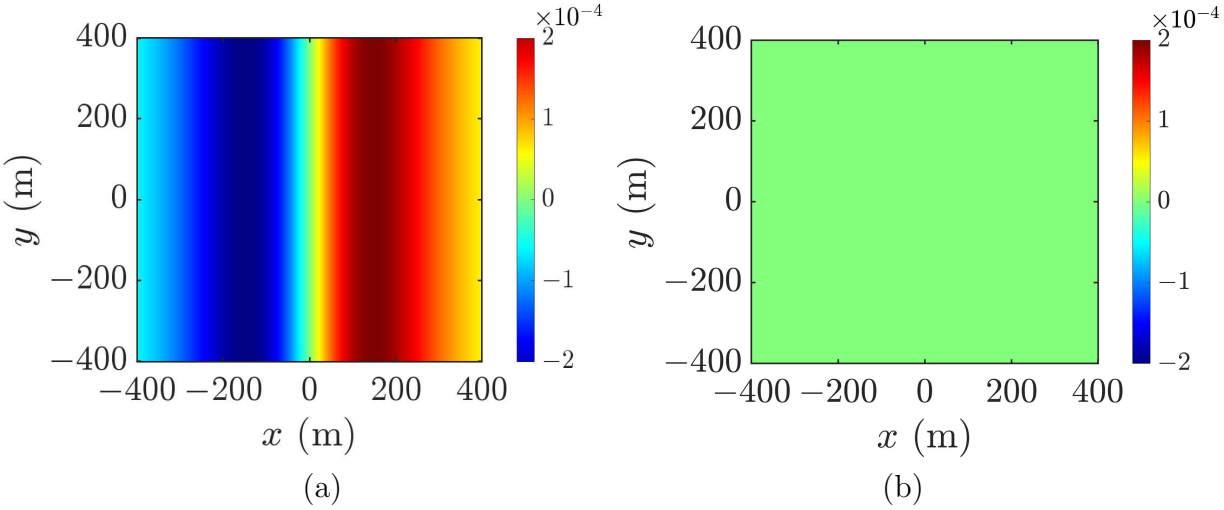

Figure 3.8: Contribution of internal wave in (2.26), simulated with parameters of event 1 in Table 4.1, (a) $\phi_{\text{iw}} = 0$, (b) $\phi_{\text{iw}} = \pi/2$.

Fig.3.8 shows the contribution of an internal wave to the NRCS from the sea surface, specified by the third term in (2.26). It is observed that its contribution to NRCS is not discernible at $\phi_{\text{iw}} = \pi/2$, which implies that an internal wave moving in parallel to the satellite flying direction cannot be revealed from the XTI-SAR image.

3.6.2 Baseline Decorrelation and Center Frequency Shift

Fig.3.9 shows a schematic of look-angle difference $\Delta\theta$ between two satellites separated by a baseline $b_\perp$. If the baseline $b_\perp$ is larger than a critical baseline $b_{\perp c}$, $\Delta\theta$ will be too large that the images acquired from main satellite and secondary satellite become decorrelated [53],

doi:10.6342/NTU202501333

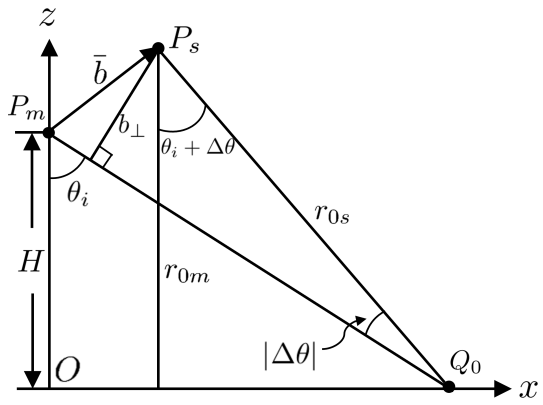

Figure 3.9: Range spectral shift due to look-angle difference, $\Delta\theta \simeq -b_\perp / r_{0m}$, $b_\perp \ll H$.

sabotaging the XTI-SAR imaging method. As listed in Table 4.2, $b_\perp = 1500$ m, which is only 0.2 % that of $H = 525$-572 km, satisfying the approximation of $b_\perp \ll H$.

The ground-range (x) component of Bragg-resonant wavenumber viewed from the main satellite is [44]

$$k_{xm}(f) = 2k \sin\theta_i = \frac{4\pi f \sin\theta_i}{c}$$

and the spectral bandwidth is

$$B_{xm} = \frac{4\pi B_r \sin\theta_i}{c}$$

Similarly, the x component of Bragg-resonant wavenumber viewed from the secondary satellite is

$$k_{xs}(f) = 2k \sin(\theta_i + \Delta\theta) \simeq \frac{4\pi f(\sin\theta_i + \Delta\theta \cos\theta_i)}{c} \tag{3.18}$$

and the spectral bandwidth is

$$B_{xs} = \frac{4\pi B_r \sin(\theta_i + \Delta\theta)}{c} \simeq B_{xm} + \frac{4\pi B_r \Delta\theta \cos\theta_i}{c} \tag{3.19}$$

doi:10.6342/NTU202501333

The main signal and the secondary signal become completely uncorrelated if the two spectra are separated [54], namely, $|k_{xs}(f_0) - k_{xm}(f_0)| \geq B_{xm}$, which implies

$$|\Delta\theta| \geq \frac{B_r \tan\theta_i}{f_0} \text{ or } \frac{b_\perp}{r_{0m}} \geq \frac{B_r \tan\theta_i}{f_0} \tag{3.20}$$

A critical baseline $b_{\perp c}$ is determined from the equal sign in (3.20) as

$$b_{\perp c} = \frac{\lambda r_{0m} B_r \tan\theta_i}{c} = \frac{0.886 \lambda r_{0m}}{2\Delta x \cos\theta_i} \tag{3.21}$$

where Δx is the horizontal resolution in x direction. The effects of baseline decorrelation can be mitigated by applying a range spectral filter [54] or by choosing a baseline shorter than $b_{\perp c}$.

3.6.3 Trade-off between Horizontal Resolution and Vertical Accuracy

The choices of look angle and mean-filter size affect the trade-off between horizontal resolution and height accuracy. The first dilemma comes from the choice of look angle. The height error $\delta\zeta$ is related to the phase error $\delta\phi$ as [55]

$$\delta\zeta = \frac{\lambda_0 r_{0m} \sin\theta_i}{2\pi b_\perp} \delta\phi \tag{3.22}$$

which implies that smaller look angle θ_i results in lower height error, complying with that of InSAR altimetry. On the other hand, the horizontal resolution of SAR imaging with

doi:10.6342/NTU202501333

bandwidth B_r is given by [56]

$$\Delta x = 0.886 \frac{c}{2B_r \sin\theta_i} \tag{3.23}$$

which implies that finer horizontal resolution is achieved at larger look angle, complying with that of conventional XTI-SAR.

The random phase can be smeared out with larger mean filter, achieving better height accuracy. However, the horizontal resolutions w_x and w_y are related to the mean-filter widths N_{wr} and N_{wa} as

$$w_x = N_{wr}\Delta x, w_y = N_{wa}\Delta y \tag{3.24}$$

where Δx and Δy are the intrinsic resolution of SAR imaging in x and y directions, respectively. Choosing larger N_{wr} and N_{wa} results in better height accuracy but worse horizontal resolution, possibly smears out subtle internal-wave signature, as will be demonstrated in Chapter 4.6. The proposed method of collecting data from multiple satellite pairs can be used to preserve the height accuracy, without compromising the horizontal resolution.

doi:10.6342/NTU202501333

Chapter 4

Simulations and Discussion

Table 4.1 lists the parameters of two internal-wave events. The first event was recorded with TerraSAR-X on April 22, 2010, near Dongsha Atoll in the South China Sea [8]. The upper-layer depth h_1 is estimated from the Doppler velocity anomaly acquired with ATI imaging technique. The ocean depth h is estimated from nautical charts. The normalized density difference $\Delta\rho/\rho$ is derived from the WOA18 [57]. The half-width of internal wave is estimated as $\ell = 224$ m by using (2.4).

The internal wave in the second event was captured in a SAR image with marine X-band radar in the Mid-Atlantic Bight (MAB) [58]. Relevant parameters are derived from the in-

Table 4.1: Parameters of internal-wave event.

parameter	symbol	case 1	case 2
upper-layer depth	h_1	80 m	12.5 m
lower-layer depth	h_2	370 m	62.5 m
normalized density difference	$\Delta\rho/\rho$	2.4×10^{-3}	3.1×10^{-3}
IW maximum amplitude	η_0	80 m	16.6 m
IW propagation direction	ϕ_{iw}	0°	0°
wind speed	U_{10}	4−9 m/s	3 m/s
wind direction	ϕ_w	30°	30°

doi:10.6342/NTU202501333

Table 4.2: Parameters for reconstructing internal-wave signatures with multiple satellite pairs.

parameter	symbol	value
carrier frequency	f_c	13.56 GHz
bandwidth	B_r	101.2/103.3/105.5 MHz
wavelength	λ_0	0.022 m
incident angle	θ_i	39°/40°/41°
polarization		hh
squint angle	θ_{sq}	0°
platform altitude	H	525/547/559/572 km
platform velocity	v_s	7569-7594 m/s
range sampling freq.	F_r	$1.2B_r$
pulse repetition freq.	F_a	3700/3800 Hz
pulse width	T_r	1.5 μs
range samples	N_r	1024
azimuth samples	N_a	2048
aperture time	T_a	0.44-0.49 s
parallel baseline	$b_{\parallel}$	0 m
perp. baseline	$b_{\perp}$	1500 m
ground range reso.	Δx	2 m
azimuth reso.	Δy	2 m
oversampling ratio	N_s	16
# sub-images	$N_{rt} \times N_{at}$	8×8
mean filter width	$N_{wr} \times N_{wa}$	7×7
# satellite pairs	N	12

situ data of temperature moorings. The half-width of internal wave is estimated as $\ell = 31.3$ m by using (2.4).

Table 4.2 lists the parameters of multiple satellite pairs. The look angle of each satellite pair lies between 39 and 41°.

Table 4.3 lists the azimuth angles of 12 satellite pairs, looking into a target area in the simulations. Referring to the Starlink constellation [36], four satellite altitudes of 525, 547, 559 and 572 km are chosen. The XTI-SAR imaging technique is applied at three look angles,

doi:10.6342/NTU202501333

Table 4.3: Azimuth angle ϕ_s of satellite pairs.

$H \setminus \theta_i$	39°	40°	41°
525 km	0°	120°	240°
547 km	30°	150°	270°
559 km	60°	180°	300°
572 km	90°	210°	330°

and the satellite pairs at a given altitude are uniformly spaced in azimuth angle.

In this work, the received signals for SAR imaging are simulated under a stop-and-go assumption. The satellite position and the ocean surface are approximated as frozen during the emission of each individual pulse. The pulse repetition frequency F_a is related to the azimuth resolution Δy as $\Delta y = v_s \Delta\eta = v_s/F_a$ [56], where $\Delta\eta = 1/F_a$ is the pulse repetition interval. As a satellite flies higher, its speed v_s becomes lower [59], and its F_a should be decreased to maintain the same Δy. Thus, F_a is set to 3700 Hz at orbital height of $H = 572$ km, and 3800 Hz at other orbital heights of $H = 525, 547, 559$ km. The coherent processing interval is $T_a = 0.44$-0.49 s, pending on the orbital height of satellite pair. Hence, the horizontal resolution of each SAR image achieved with the default parameters listed in Table 4.2 is close to $\Delta x = \Delta y = 2$ m.

The ocean wave driven by wind is simulated with a Pierson-Moskowitz spectrum [46]. The target area is first segmented into multiple pixels. Each pixel has size of 1 m $\times$ 1 m and its height is the ocean-wave height at the pixel center. The amplitude and phase of the echoed signal from each pixel are derived in terms of the NRCS and the slant range,

doi:10.6342/NTU202501333

respectively, from that pixel. The NRCS value attributed to each pixel is computed with eqn. (2.26). The received signal at each slow time instant is the sum of echoed signals from all the pixels. Under the strongest wind of $U_{10} = 9$ m/s considered in this work, the dominant wind wave component moves at phase speed of $c_p \simeq 11.01$ m/s in deep water and traverses about 6 m during a coherent processing interval of $T_a = 0.44$-0.49 s. A range-Doppler algorithm is applied to reconstruct a SAR image from the received signals at each satellite [56]. The proposed XTI-SAR imaging method is then applied to the two SAR images derived from one pair of satellites to reconstruct a sea-surface profile, which is the superposition of wind-wave profile and internal-wave signature.

To assess the performance of reconstructing internal-wave signatures, define a root-mean-square error (RMSE) between the true height profile ζ and its reconstructed counterpart $\tilde{\zeta}$ as

$$\mathrm{RMSE}(\tilde{\zeta}, \zeta) = \sqrt{\frac{1}{N_x N_y} \sum_{n=1}^{N_y} \sum_{m=1}^{N_x} \left(\tilde{\zeta}[m,n] - \zeta[m,n]\right)^2} \tag{4.1}$$

which is abbreviated as RMSE. If the internal-wave signature in (2.9) is used as a true profile of ζ_{iw}, the resulting $\mathrm{RMSE}(\tilde{\zeta}, \zeta_{\mathrm{iw}})$ is abbreviated as $\mathrm{RMSE}_{\mathrm{iw}}$.

Fig.4.1 shows the snapshots of sea-surface profile simulated with the parameters listed in Table 4.1, with $U_{10} = 4$ m/s, and the XTI-SAR images reconstructed with the parameters listed in Table 4.2. Fig.4.1(a) shows that the internal-wave signature manifests a stripe-like

doi:10.6342/NTU202501333

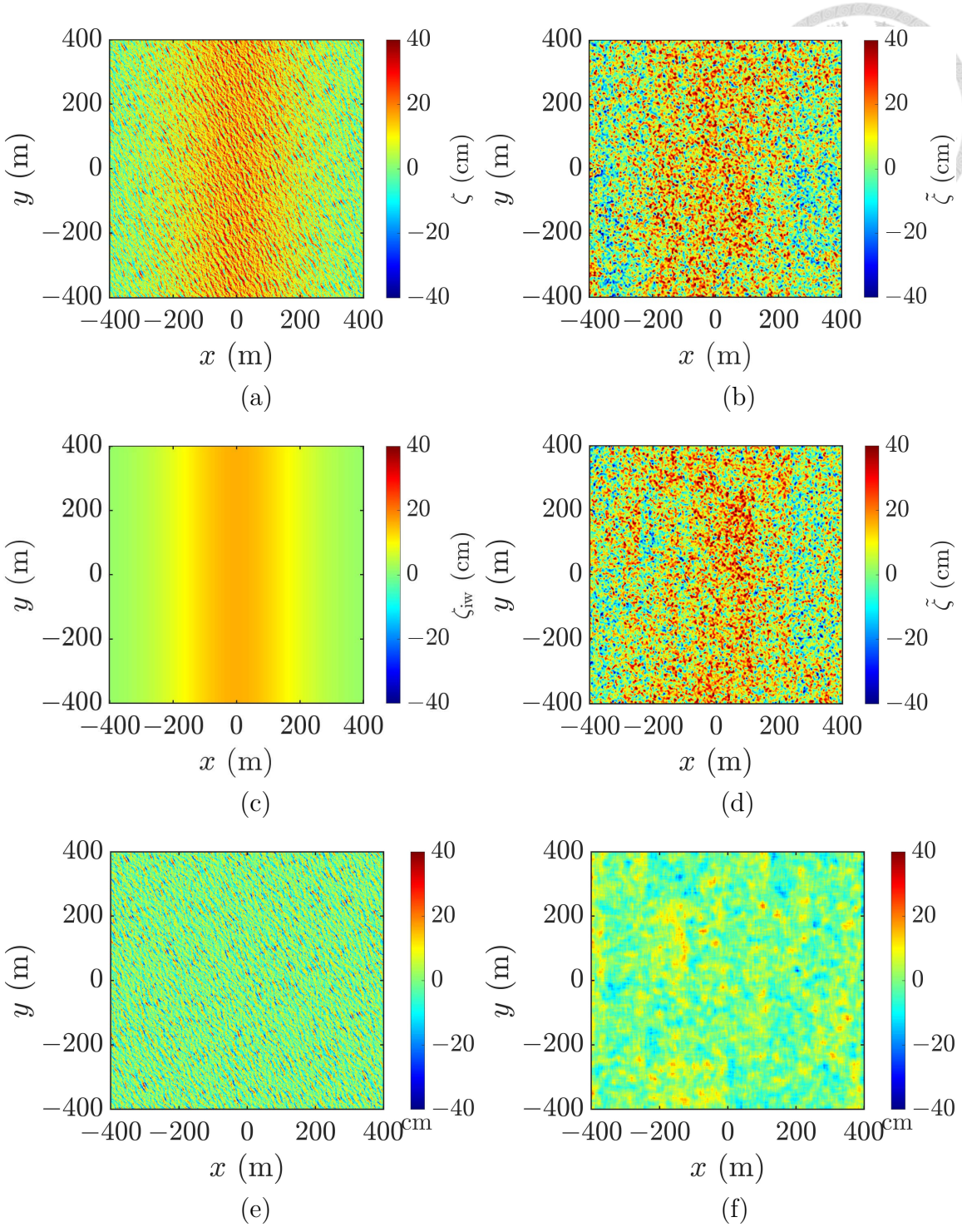

Figure 4.1: Snapshots of sea-surface profile simulated with parameters of event 1 in Table 4.1, $U_{10} = 4$ m/s, and XTI-SAR images acquired with parameters listed in Table 4.2 and one satellite pair, (a) internal-wave signature immersed in wind wave, (b) reconstructed image of (a), RMSE = 15.38 cm, (c) internal-wave signature, (d) reconstructed image of (c), RMSE = 13.33 cm, (e) flat surface, (f) reconstructed image of (e), RMSE = 13.03 cm.

doi:10.6342/NTU202501333

pattern. Fig.4.1(b) shows the reconstructed image, where the features of wind wave are suppressed but the stripe-like pattern is sputtered with artificial speckles.

To trace possible cause of these speckles, a sea-surface profile containing only internal-wave signatures is simulated as shown in Fig.4.1(c). However, Fig.4.1(d) shows that speckles sustain in the reconstructed XTI-SAR image, implying that the wind-wave is not the main cause of these speckles. Fig.4.1(e) shows a flat surface and Fig.4.1(f) shows its reconstructed image with the parameters listed in Table 4.2. The enduring speckles are attributed to the XTI-SAR imaging process.

Note that the sea-surface profile is updated about once every 0.1 s to compute the echoed signals, from which SAR images are acquired and further processed to reconstruct the surface height images shown in Figs.4.1(b), 4.1(d) and 4.1(f), respectively.

4.1 Velocity Bunching Effect

The sea surface movement arouses velocity bunching effect, inducing azimuthal shift to the echoed signals [44]. Generally speaking, a rising surface patch and a falling surface patch shift the echoed signals toward positive and negative azimuth directions, respectively, mapping their horizontal positions to incorrect pixels in a SAR image.

In this work, the sea surface is modeled as a grid of point targets which move up and down in z-direction as wind wave and internal-wave signature pass by. The motion of sea

doi:10.6342/NTU202501333

surface profile induces azimuth shift, with the true azimuth position y and reconstructed azimuth position y' related by $y' = y + r_0(x)v_r/v_s$, where $r_0(x)$ is the slant range from the satellite to a point target located at (x, y), and v_r is the radial velocity component of the point target toward the satellite. A derivation of this relation is presented in the Appendix, which is consistent with the discussions about velocity bunching effect on SAR images of ocean wave [60]-[65].

To better demonstrate the velocity bunching effect, the sea-surface profile is updated once every 32 pulse repetition intervals (about 0.007 s) to compute the echoed signals, from which the SAR image is reconstructed. Fig.4.2(a) shows a SAR image of sea-surface profile with internal-wave signature immersed in wind wave under $U_{10} = 4$ m/s, and Fig.4.2(c) shows the sea-surface profile reconstructed with the XTI-SAR imaging method. The XTI-SAR image manifests the internal-wave signature more obvious that its counterpart SAR image. Similarly, Fig.4.2(b) shows a SAR image of sea-surface profile with internal-wave signature on a calm sea, and Fig.4.2(d) shows the sea-surface profile reconstructed with the XTI-SAR imaging method, in which the internal-wave signature is better discernible than in its counterpart SAR image.

The SAR images in Figs.4.2(a) and 4.2(b) manifest highly random features, which is confirmed by the fact that the autocorrelation function of either image concentrates around

doi:10.6342/NTU202501333

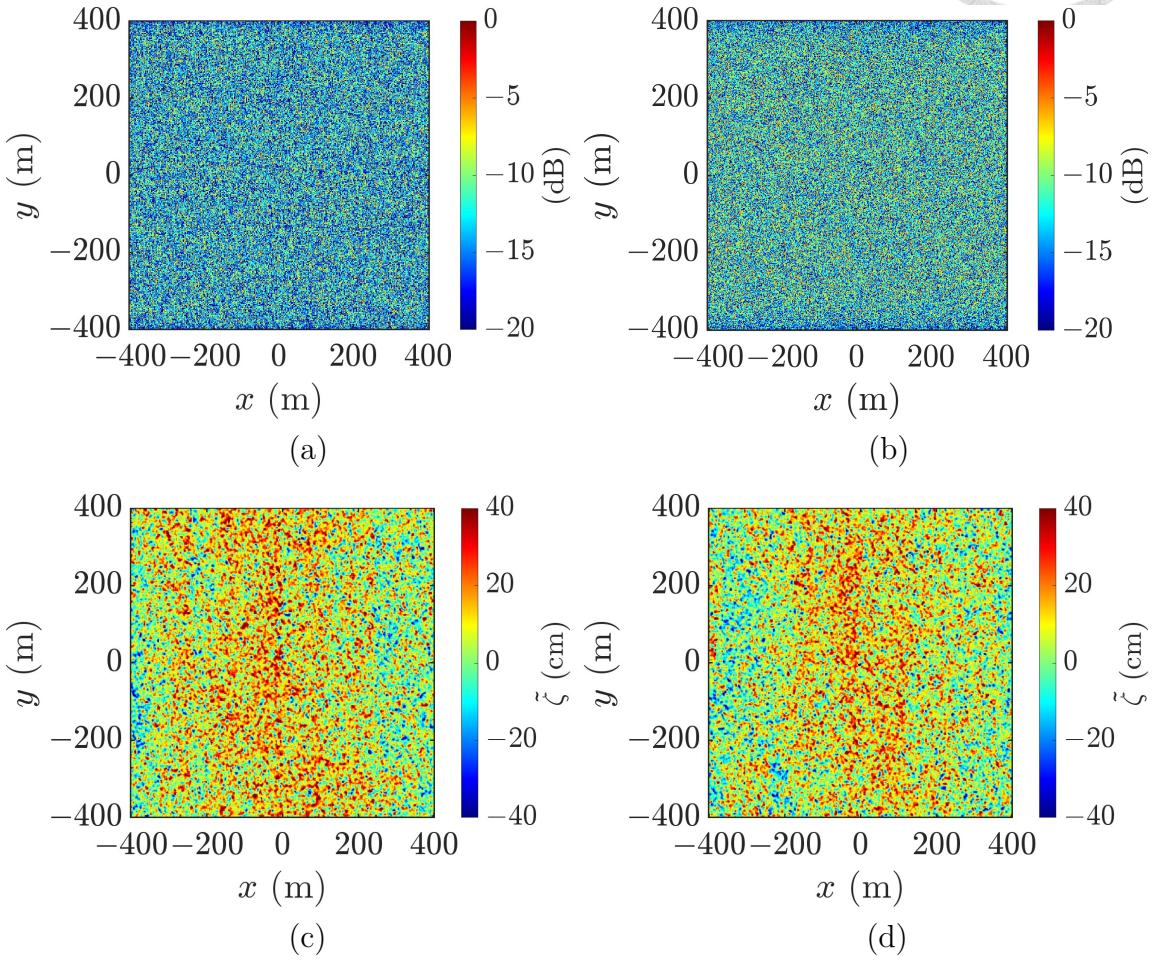

Figure 4.2: Simulated images with enhanced velocity bunching effect: (a) SAR image of sea-surface profile with internal-wave signature immersed in wind wave under $U_{10} = 4$ m/s, (b) SAR image of sea-surface profile with internal-wave signature, (c) XTI-SAR image of sea-surface profile with internal-wave signature immersed in wind wave under $U_{10} = 4$ m/s, RMSE = 16.28 cm, (d) XTI-SAR image of sea-surface profile with internal-wave signature, RMSE = 13.52 cm.

doi:10.6342/NTU202501333

the origin.

To examine the velocity bunching effect on the proposed XTI-SAR imaging method, Fig.4.2(c) is compared with Fig.4.1(b), and Fig.4.2(d) is compared with Fig.4.1(d). Visual inspection reveals little difference. Note that the sea-surface profile is updated about once every 0.1 s in Fig.4.1 while once every 32 pulse repetition intervals (about 0.007 s) in Fig.4.2 to fully demonstrate the sea-surface movement. In the latter case, the RMSE values slightly increase from 15.38 cm to 16.28 cm and from 13.33 cm to 13.52 cm, respectively. The impact of velocity bunching effect on the final XTI-SAR images is not prominent.

Fig.4.3 shows the height difference $\Delta\zeta$ between reconstructed profile and original profile, where $\Delta\zeta[m,n] = \tilde{\zeta}[m,n] - \zeta[m,n]$. Fig.4.3(a) shows the height difference between Fig.4.1(b) and Fig.4.1(a), with internal-wave signature immersed in wind wave under $U_{10} = 4$ m/s. The ocean wave movement is updated at rate much lower than F_a, hence the velocity bunching effect is not as obvious as it should have been, and RMSE = 15.38 cm. Fig.4.3(b) shows the height difference between Fig.4.2(c) and Fig.4.1(a), where the ocean wave movement is updated at rate of $F_a/32$, hence the velocity bunching effect is well manifested, and RMSE = 16.28 cm. Fig.4.3(c) shows the height difference between Fig.4.1(f) and Fig.4.1(e), with regard to a flat surface profile, where Fig.4.1(f) can be viewed as some kind of intrinsic noise attributed to the radar parameters adopted to acquire an XTI-SAR image, and RMSE

doi:10.6342/NTU202501333

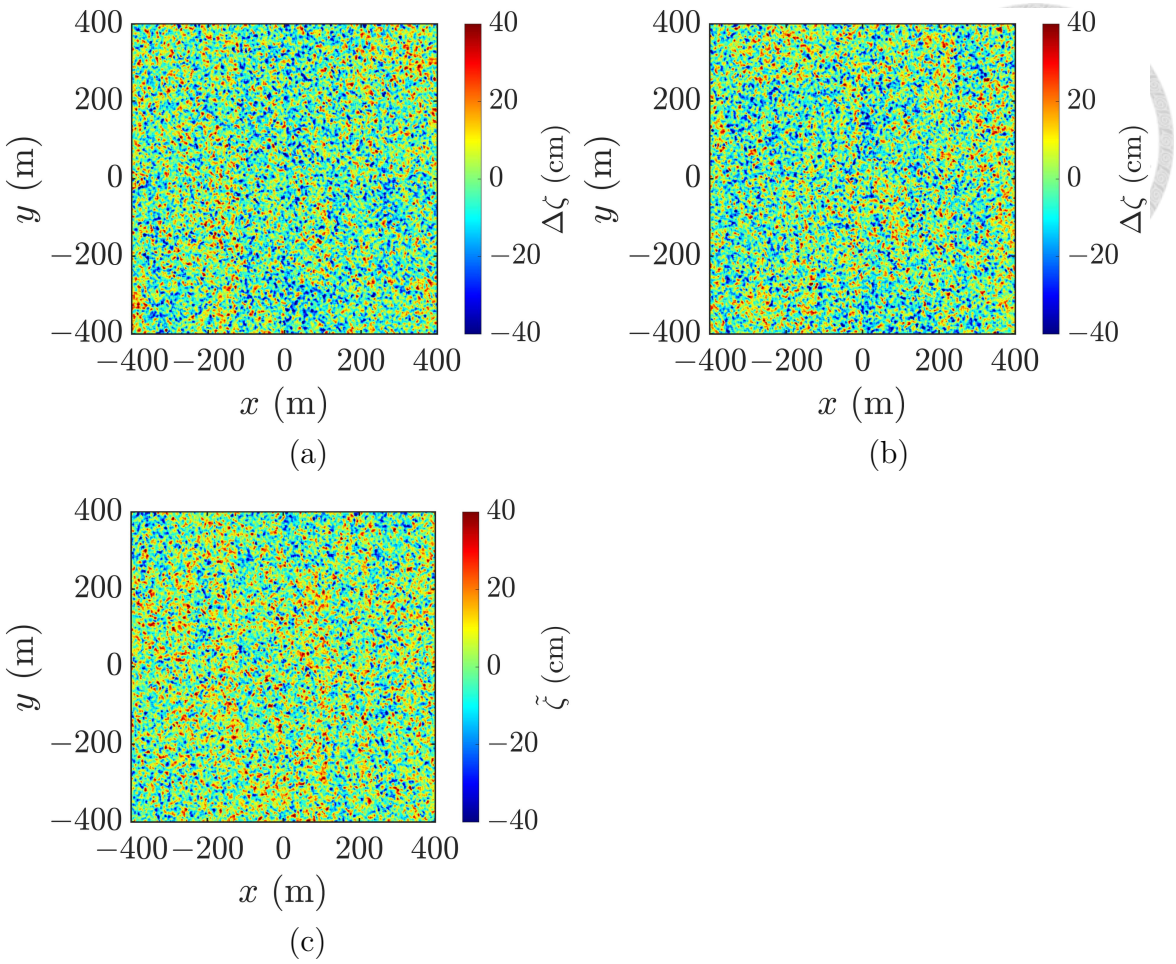

Figure 4.3: Height difference $\Delta\zeta$ between reconstructed profile and original profile, (a) $\Delta\zeta$ between Fig.4.1(b) and Fig.4.1(a), RMSE = 15.38 cm, (b) $\Delta\zeta$ between Fig.4.2(c) and Fig.4.1(a), RMSE = 16.28 cm, (c) $\Delta\zeta$ between Fig.4.1(f) and Fig.4.1(e), RMSE = 13.03 cm.

= 13.03 cm.

In short, the RMSE increases from 13.03 cm for a flat surface to 15.38 cm for sea-surface profile under U_{10} = 4 m/s, and increases further to 16.28 cm if velocity bunching effect is well manifested. The increment of RMSE attributed to velocity bunching effect is 0.9 cm, much lower than the RMSE intrinsic to the XTI-SAR imaging method with given radar parameters.

doi:10.6342/NTU202501333

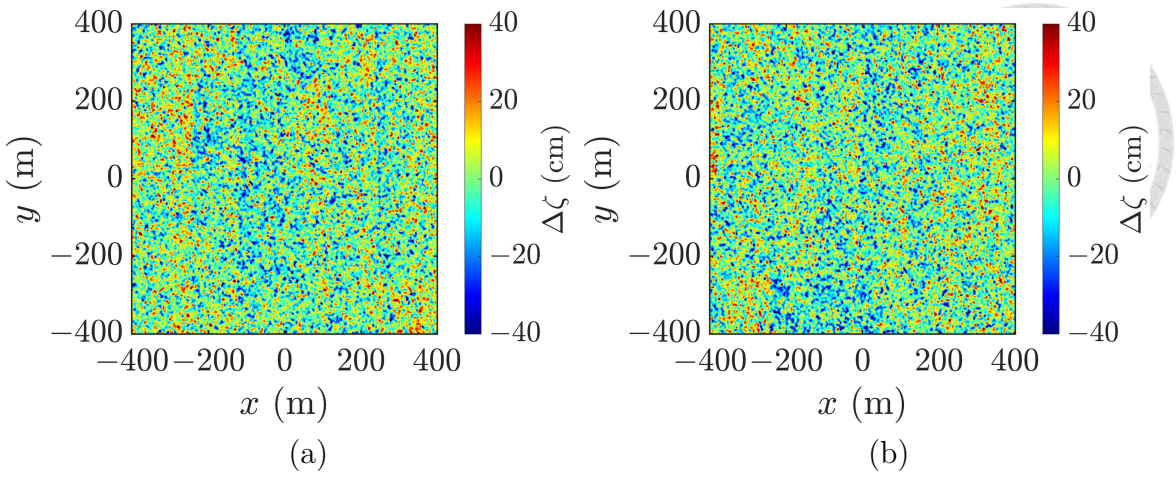

Figure 4.4: Height difference $\triangle\zeta$ between reconstructed profile and original profile of internal-wave signature, (a) $\Delta\zeta$ between Fig.4.1(d) and Fig.4.1(c), RMSE = 13.34 cm, (b) $\Delta\zeta$ between Fig.4.2(d) and Fig.4.1(c), RMSE = 13.52 cm.

Fig.4.4 shows the height difference $\Delta\zeta$ between reconstructed profile and original profile of internal-wave signature. Fig.4.4(a) shows the height difference between Fig.4.1(d) and Fig.4.1(c). The ocean wave movement is updated at rate much lower than F_a, and RMSE = 13.34 cm. Fig.4.4(b) shows the height difference between Fig.4.2(d) and Fig.4.1(c), where the ocean wave movement is updated at rate of $F_a/32$, hence the velocity bunching effect is well manifested, and RMSE = 13.52 cm.

Similar to Fig.4.3, the RMSE increases from 13.03 cm for a flat surface to 13.34 cm when an internal-wave signature appears, and further increases to 13.52 cm if velocity bunching effect is well manifested. The increment of RMSE attributed to velocity bunching effect is 0.18 cm, much lower than the RMSE intrinsic to the XTI-SAR imaging method with given radar parameters. Thus, the velocity bunching effect is not prominent in this work.

doi:10.6342/NTU202501333

4.2 Effect of Baseline

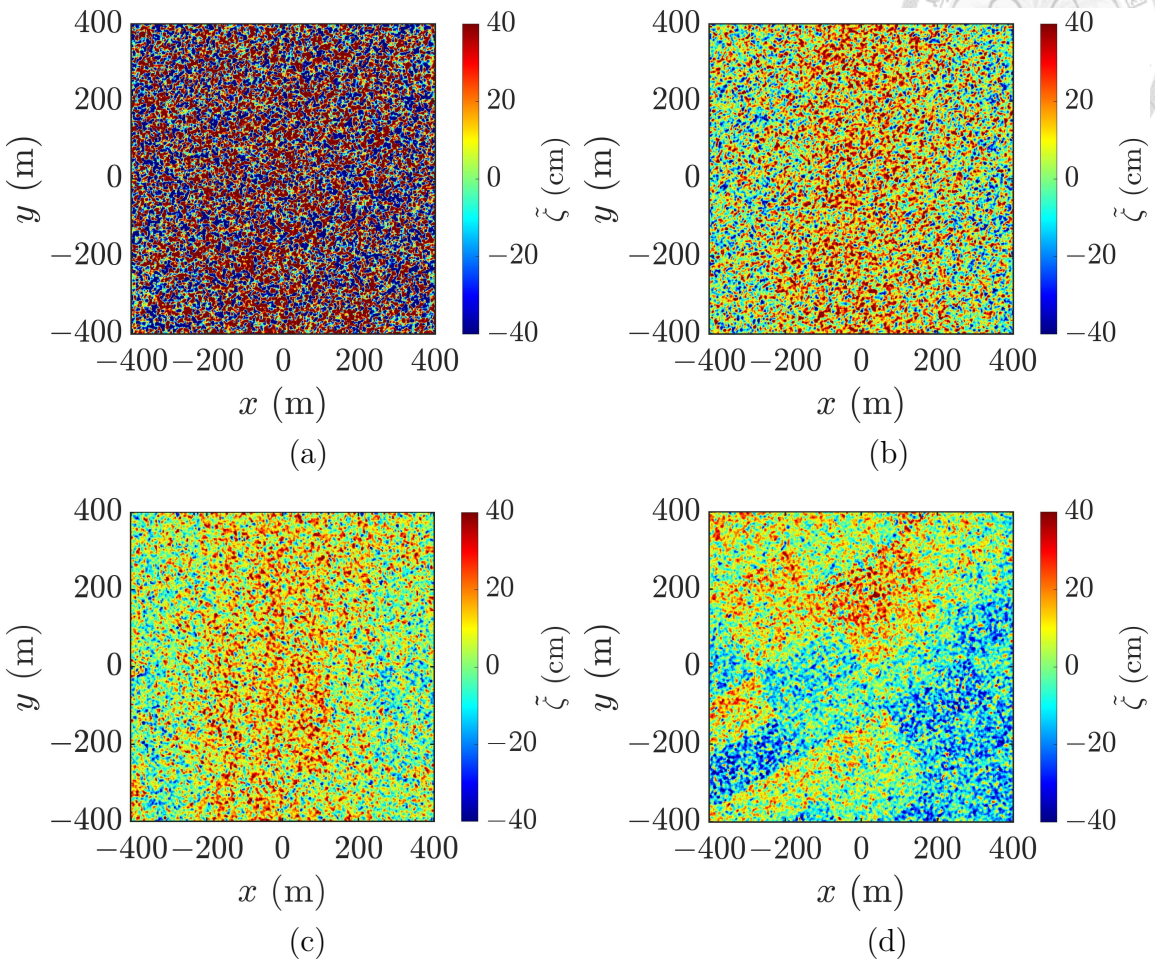

Figure 4.5: XTI-SAR images of sea-surface profile simulated with parameters of event 1 in Table 4.1, $U_{10} = 4$ m/s, acquired with default parameters in Table 4.2 and different perpendicular baselines, (a) $b_\perp = 100$ m, RMSE = 60.53 cm, $\text{RMSE}_{\text{iw}} = 60.08$ cm, (b) $b_\perp = 800$ m, RMSE = 19.86 cm, $\text{RMSE}_{\text{iw}} = 18.30$ cm, (c) $b_\perp = 1500$ m, RMSE = 15.69 cm, $\text{RMSE}_{\text{iw}} = 13.75$ cm, (d) $b_\perp = 3000$ m, RMSE = 18.92 cm, $\text{RMSE}_{\text{iw}} = 16.94$ cm.

As was discussed in Chapter 3.6.2, longer baseline may bring about decorrelation and deteriorate the acquired image. Fig.4.5 shows the XTI-SAR images of the sea-surface profile in Fig.4.1(a), reconstructed with different $b_\perp$s and the default parameters in Table 4.2.

Fig.4.5(a) shows the reconstructed image with $b_\perp = 100$ m, displaying no traces of

doi:10.6342/NTU202501333

internal-wave signatures. Fig.4.5(b) shows that by increasing baseline to $b_\perp = 800$ m, silhouette of internal-wave signature emerges. Fig.4.5(c) shows that the speckles are reduced with longer $b_\perp$. Further increase of $b_\perp$ leads to baseline decorrelation. As shown in Fig.4.5(d), the striped pattern of internal-wave signature disappears, with RMSE and RMSE_{iw} increased to 18.92 cm and 16.94 cm, respectively.

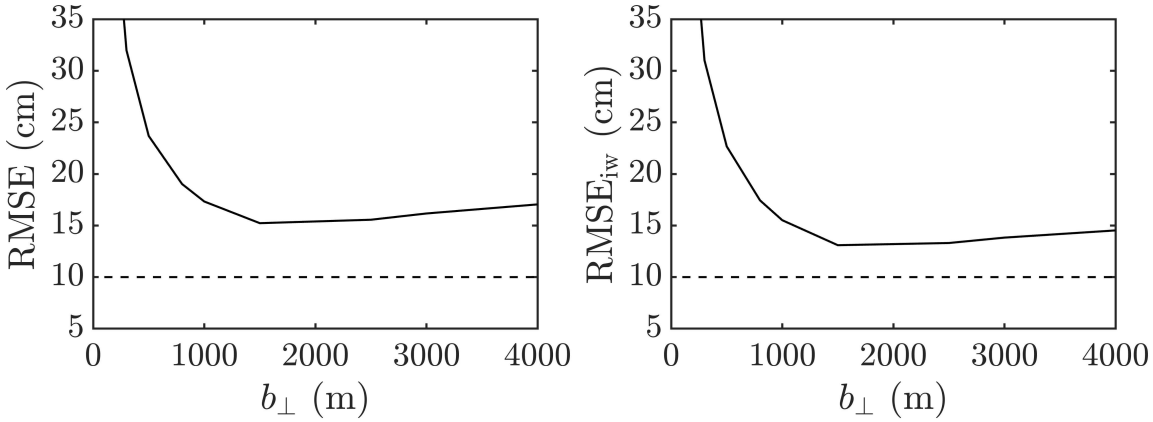

Figure 4.6: Effects of $b_\perp$ on (a) RMSE and (b) RMSE_{iw} of reconstructed images of Fig.4.1(a).

Fig.4.6 shows the trends of RMSE and RMSE_{iw}, respectively, versus $b_\perp$. It is observed that both RMSE and RMSE_{iw} drop rapidly with increasing $b_\perp$ till $b_\perp = 1500$ m, then gently rises if $b_\perp$ is further increased. Thus, $b_\perp = 1500$ m is adopted as a default parameter in the subsequent simulations.

4.3 Effect of Mean Filter Size

A mean filter of size $N_{wr} \times N_{wa}$ is commonly applied on the phase image to mitigate speckles in the resulting surface-height profile, at the cost of enlarging the horizontal resolution

doi:10.6342/NTU202501333

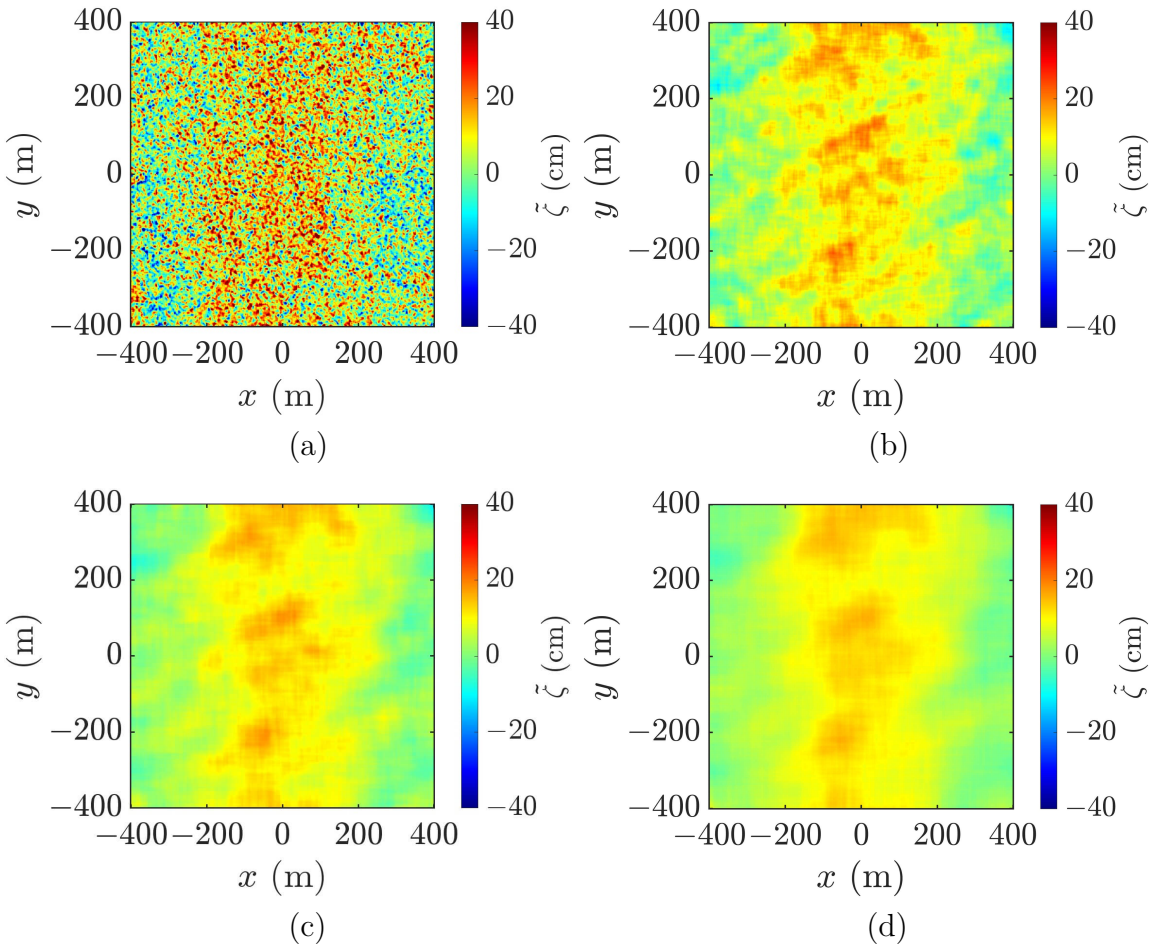

Figure 4.7: XTI-SAR images of a sea-surface profile acquired with default parameters in Table 4.2 and different mean-filter sizes, (a) $N_{wr} = 7$, $(w_x, w_y) = (14, 14)$ m, RMSE = 15.69 cm, $\text{RMSE}_{\text{iw}} = 13.75$ cm, (b) $N_{wr} = 37$, $(w_x, w_y) = (74, 74)$ m, RMSE = 9.79 cm, $\text{RMSE}_{\text{iw}} = 3.98$ cm, (c) $N_{wr} = 67$, $(w_x, w_y) = (134, 134)$ m, RMSE = 9.44 cm, $\text{RMSE}_{\text{iw}} = 3.06$ cm, (d) $N_{wr} = 97$, $(w_x, w_y) = (194, 194)$ m, RMSE = 9.32 cm, $\text{RMSE}_{\text{iw}} = 2.69$ cm.

doi:10.6342/NTU202501333

from $(\Delta x, \Delta y)$ to $(w_x, w_y) = (N_{wr}\Delta x, N_{wa}\Delta y)$. Fig.4.7 shows the reconstructed images of Fig.4.1(a), with different mean-filter sizes. It is observed that the speckles are significantly smeared by choosing larger mean-filter size. However, the striped patterns in Figs.4.7(b)-4.7(d) are distorted as compared with Fig.4.1(c).

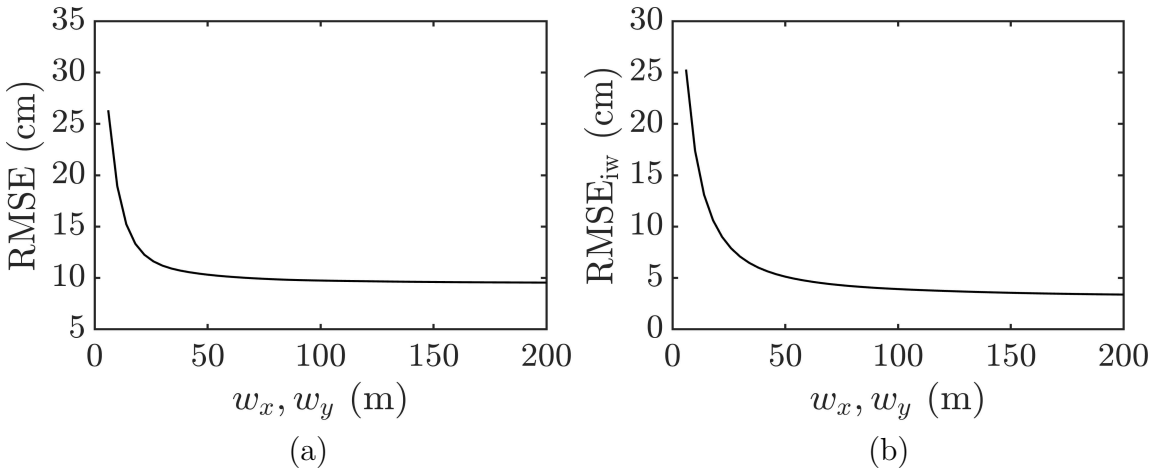

Figure 4.8: Effects of mean-filter size on (a) RMSE and (b) RMSE_{iw} of reconstructed images of Fig.4.1(a).

Fig.4.8 shows the effects of mean-filter size on RMSE and RMSE_{iw}, respectively, of reconstructed images of Fig.4.1(a). Both RMSE and RMSE_{iw} drop rapidly with filter size, gradually converge to RMSE $\simeq$ 10 cm and $\text{RMSE}_{\text{iw}} \simeq$ 3.5 cm.

4.4 Selection of Baseline, Mean-Filter Size and Satellite Pair Number

Fig.4.9 shows the sea-surface profiles of event 1 in Table 4.1, acquired with different numbers of satellite pairs. As more satellite pairs are adopted, more wind-wave features are removed and the internal-wave signatures become more discernible, as compared to Fig.4.1(c).

doi:10.6342/NTU202501333

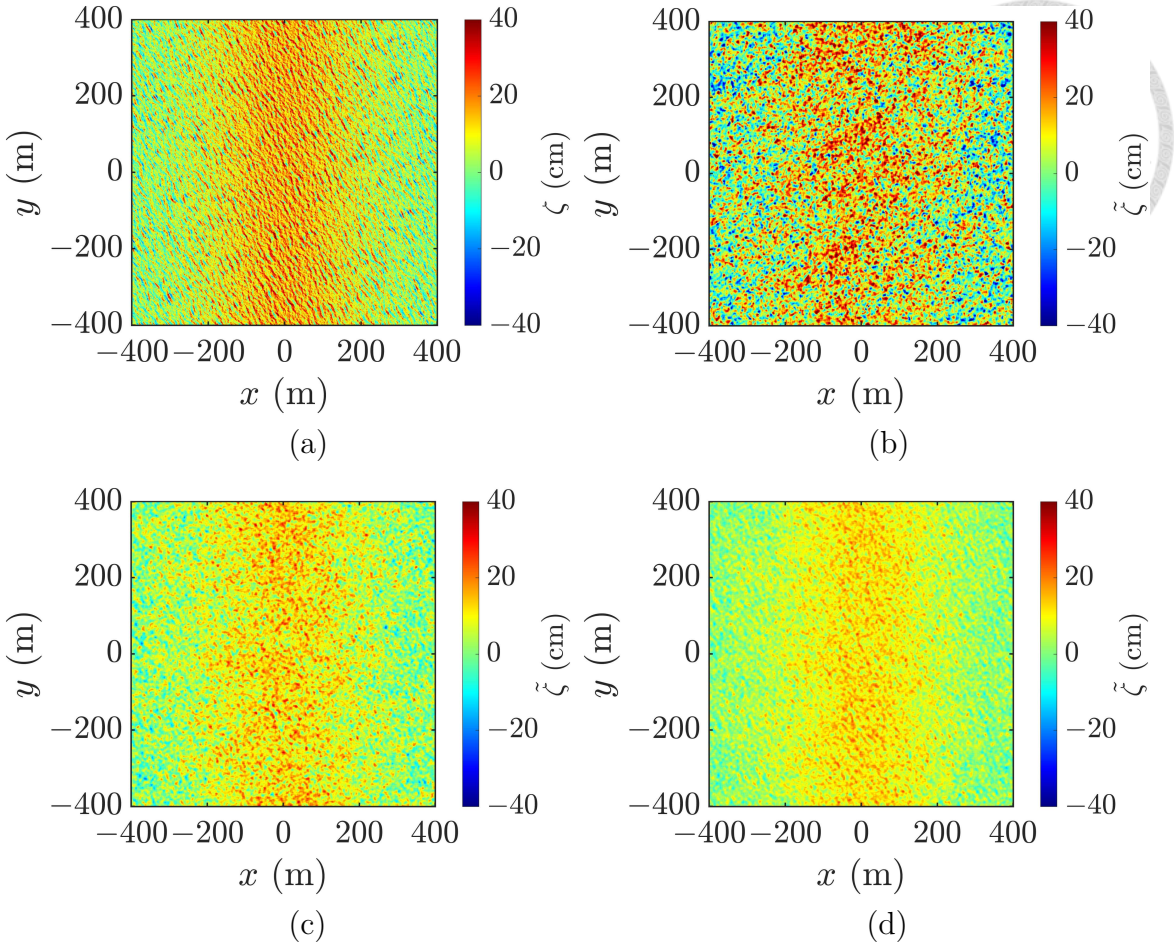

Figure 4.9: XTI-SAR images acquired from sea-surface profile of event 1 in Table 4.1, with default parameters in Table 4.2, $U_{10} = 4$ m/s, (a) simulated profile, (b) single pair, RMSE = 15.69 cm, $\text{RMSE}_{\text{iw}} = 13.75$ cm, (c) 5 pairs, RMSE = 9.80 cm, $\text{RMSE}_{\text{iw}} = 6.40$ cm, (d) 12 pairs, RMSE = 8.82 cm, $\text{RMSE}_{\text{iw}} = 4.82$ cm.

Fig.4.10 shows effects of $b_\perp$, w_x, w_y and satellite pair numbers on RMSE and RMSE_{iw}, respectively, of sea-surface profiles simulated with the parameters of event 1 in Table 4.1 and $U_{10} = 4$ m/s. The default radar parameters are listed in Table 4.2.

Irrespective of the satellite-pair number, the RMSE drops sharply with the increase of $b_\perp$, then rises gradually if $b_\perp$ is further increased. The RMSE of image acquired with one satellite pair decreases significantly as compared with that of averaging over 5 satellite pairs,

doi:10.6342/NTU202501333

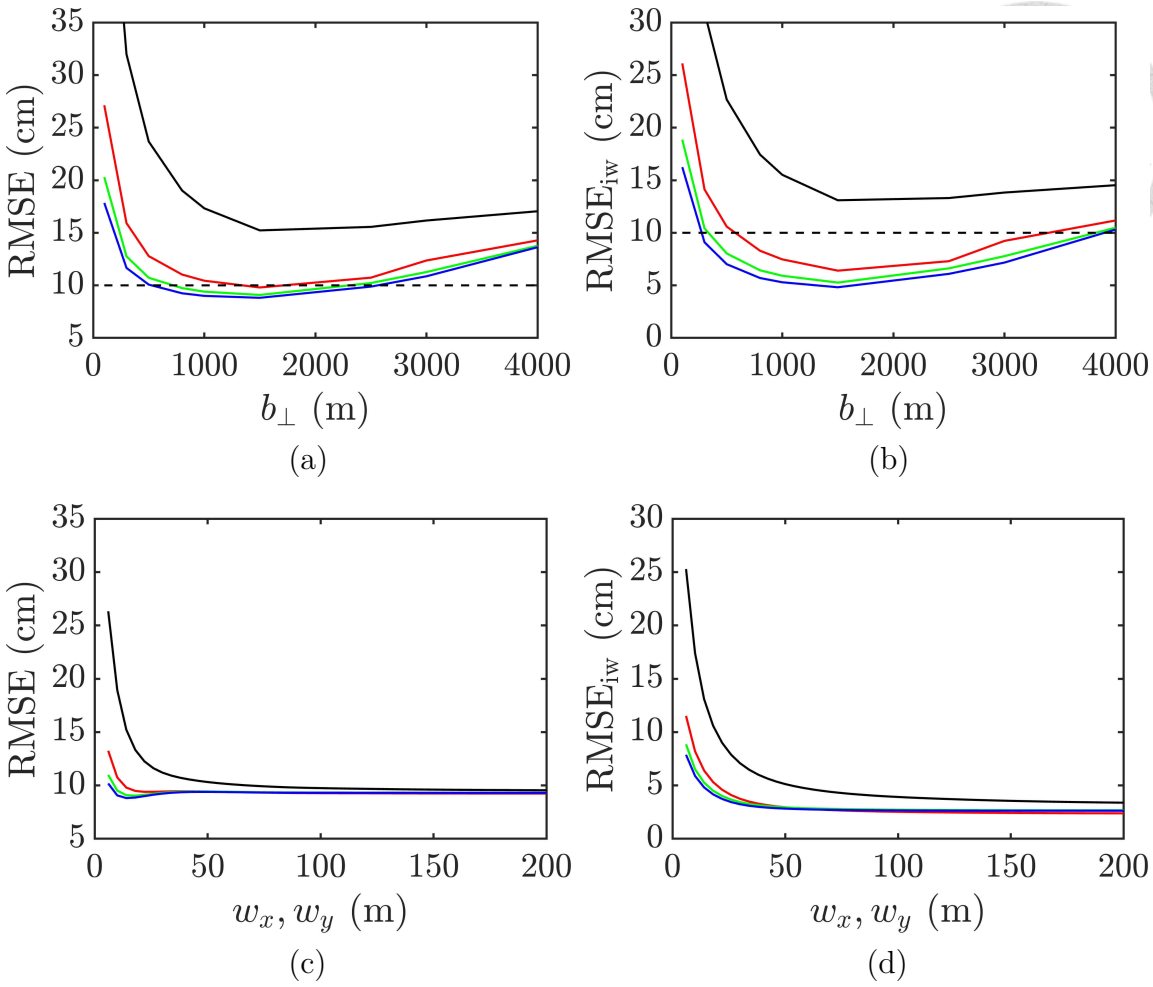

Figure 4.10: Effect of parameters on RMSE and RMSE_{iw} of sea-surface profiles simulated with parameters of event 1 in Table 4.1, $U_{10} = 4$ m/s, reconstructed with radar parameters listed in Table 4.2. Effect of (a) $b_\perp$ on RMSE, (b) $b_\perp$ on RMSE_{iw}, (c) w_x, w_y on RMSE, (d) w_x, w_y on RMSE_{iw}. ————: 1 pair, ————: 5 pairs, ————: 9 pairs, ————: 12 pairs.

and gradually converges to that of averaging over 12 satellite pairs. The variation of RMSE_{iw} versus $b_\perp$ shown in Fig.4.10(b) follows similar trend as in Fig.4.10(a).

Fig.4.10(c) shows the effect of horizontal resolution or mean-filter size on RMSE of the reconstructed sea-surface profiles. Under each number of satellite pairs, the RMSE drops sharply as w_x and w_y are increased from small number, then converges as w_x and w_y are increased to 50 m. The lowest RMSE value is achieved with $w_x = w_y = 14$ m and 12 satellite

doi:10.6342/NTU202501333

pairs.

4.5 Effect of Wind Speed

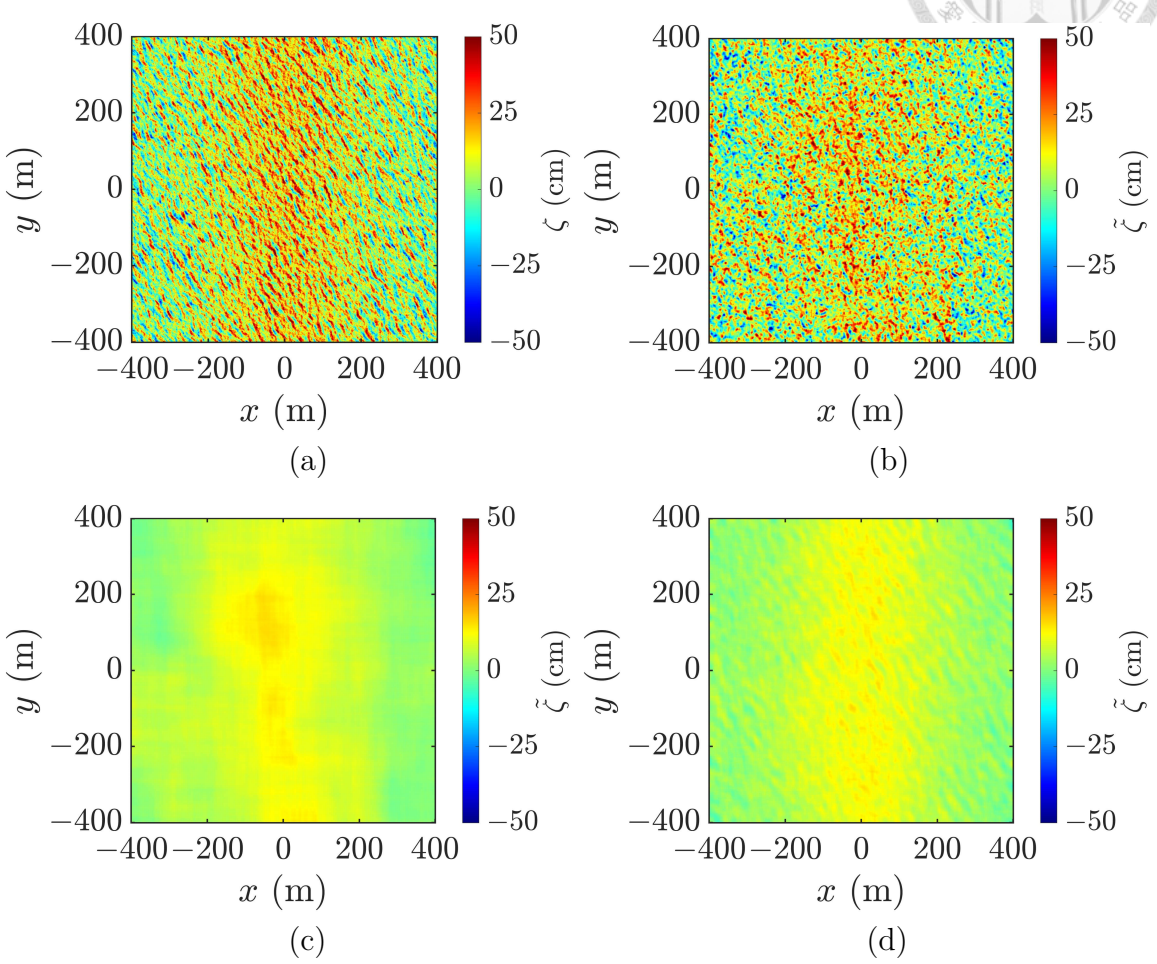

Figure 4.11: XTI-SAR images acquired from sea-surface profile of event 1 in Table 4.1, with default parameters in Table 4.2, $U_{10} = 5$ m/s, (a) simulated profile, (b) single pair, $w_x = w_y = 14$ m, RMSE = 16.84 cm, $\text{RMSE}_{\text{iw}} = 14.93$ cm, (c) single pair, $w_x = w_y = 202$ m, $\text{RMSE}_{\text{iw}} = 2.94$ cm, (d) 12 pairs, $w_x = w_y = 50$ m, $\text{RMSE}_{\text{iw}} = 3.30$ cm.

Fig.4.11 shows the XTI-SAR images of the sea-surface profile of event 1 in Table 4.1, acquired with the default parameters listed in Table 4.2 and $U_{10} = 5$ m/s. Fig.4.11(b) shows that with only one satellite pair and a small mean-filter, the stripe pattern is barely discernible. Fig.4.11(c) shows that the stripe pattern becomes discernible by increasing the

doi:10.6342/NTU202501333

size of mean filter. Fig.4.11(d) shows that similar internal-wave signatures can be recognized with smaller mean-filter size to preserve the horizontal resolution of $w_x = w_y = 50$ m by using 12 pairs of satellites.

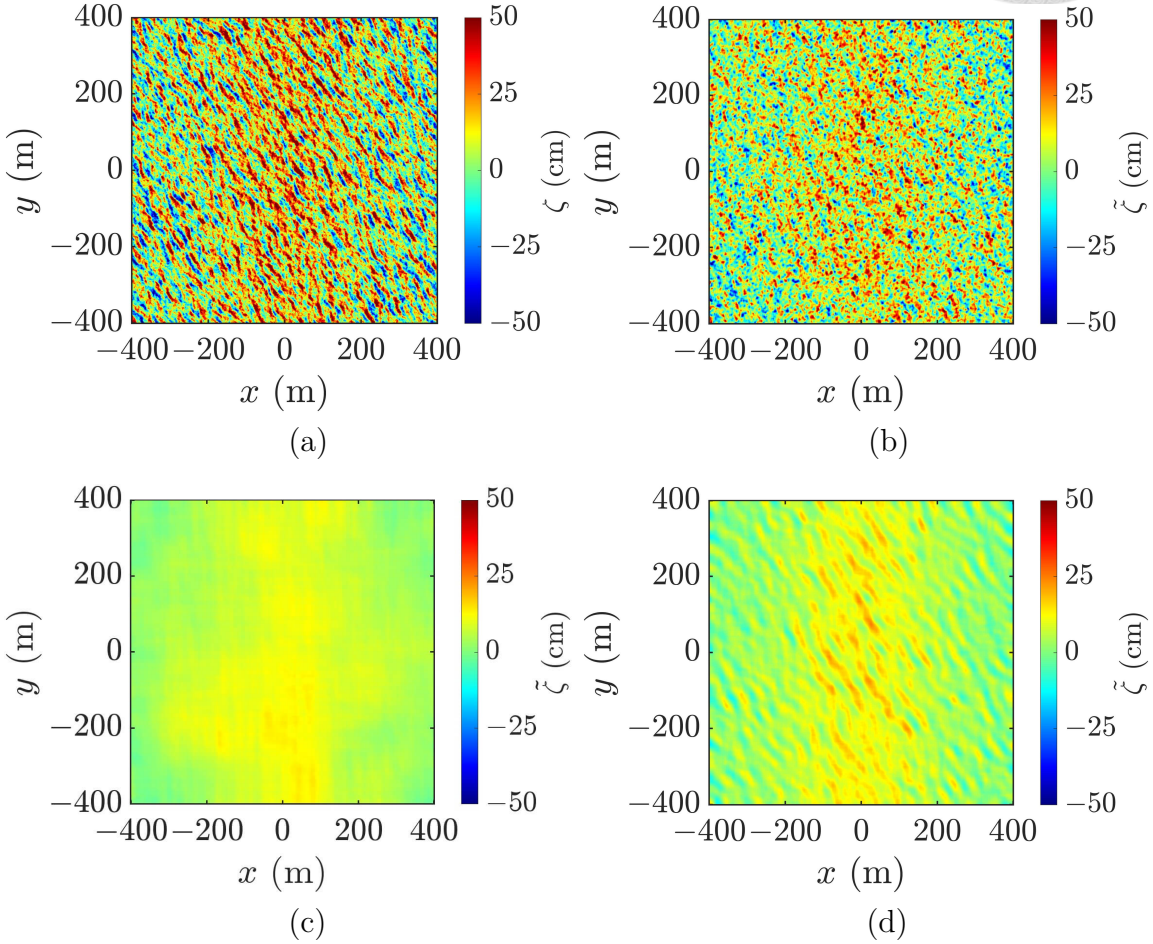

Figure 4.12: XTI-SAR images acquired from sea-surface profile of event 1 in Table 4.1, with default parameters in Table 4.2, $U_{10} = 6$ m/s, (a) simulated profile, (b) single pair, $w_x = w_y = 14$ m, RMSE = 18.29 cm, $\text{RMSE}_{\text{iw}} = 17.45$ cm, (c) single pair, $w_x = w_y = 202$ m, $\text{RMSE}_{\text{iw}} = 3.22$ cm, (d) 12 pairs, $w_x = w_y = 50$ m, $\text{RMSE}_{\text{iw}} = 4.98$ cm.

It was reported in [16] that internal-wave signatures were barely discernible at $U_{10} > 5$ m/s. Fig.4.12 shows the comparison of XTI-SAR images acquired with multiple satellite pairs and different mean-filter sizes, under $U_{10} = 6$ m/s.

doi:10.6342/NTU202501333

Fig.4.12(a) shows the simulated profile of internal-wave signatures immersed in a wind wave, under $U_{10} = 6$ m/s. Fig.4.12(b) shows the acquired XTI-SAR image with one pair of satellites. The stripe-like pattern of internal-wave signatures is recognizable, but is severely interfered by the rough sea surface.

Fig.4.12(c) shows that the stripe-like pattern is significantly enhanced by applying a mean filter of window size $w_x = w_y = 202$ m, but its shape is slightly distorted. Fig.4.12(d) shows that by applying 12 satellite pairs, the internal-wave signatures can be reconstructed at horizontal resolution about 4 times finer than that in Fig.4.12(c).

Fig.4.13(a) shows the simulated profile of internal-wave signatures immersed in a wind wave under $U_{10} = 9$ m/s, making the former completely indiscernible. Fig.4.13(b) shows that using one pair of satellites fails to manifest the internal-wave signatures. Fig.4.13(c) shows that by applying a mean filter of large size $w_x = w_y = 202$ m, faint internal-wave signatures are revealed. Although taking a larger filter size helps removing the wind waves, but the horizontal resolution is deteriorated as compared with Fig.4.13(b).

However, Fig.4.13(d) shows that using 12 pairs of satellites, followed by mean filter of size $w_x = w_y = 50$ m, fails to reveal the internal-wave signatures. Note that wind waves under $U_{10} = 9$ m/s, with wavelength about 70 m, cannot be effectively removed with the mean filter [46].

doi:10.6342/NTU202501333

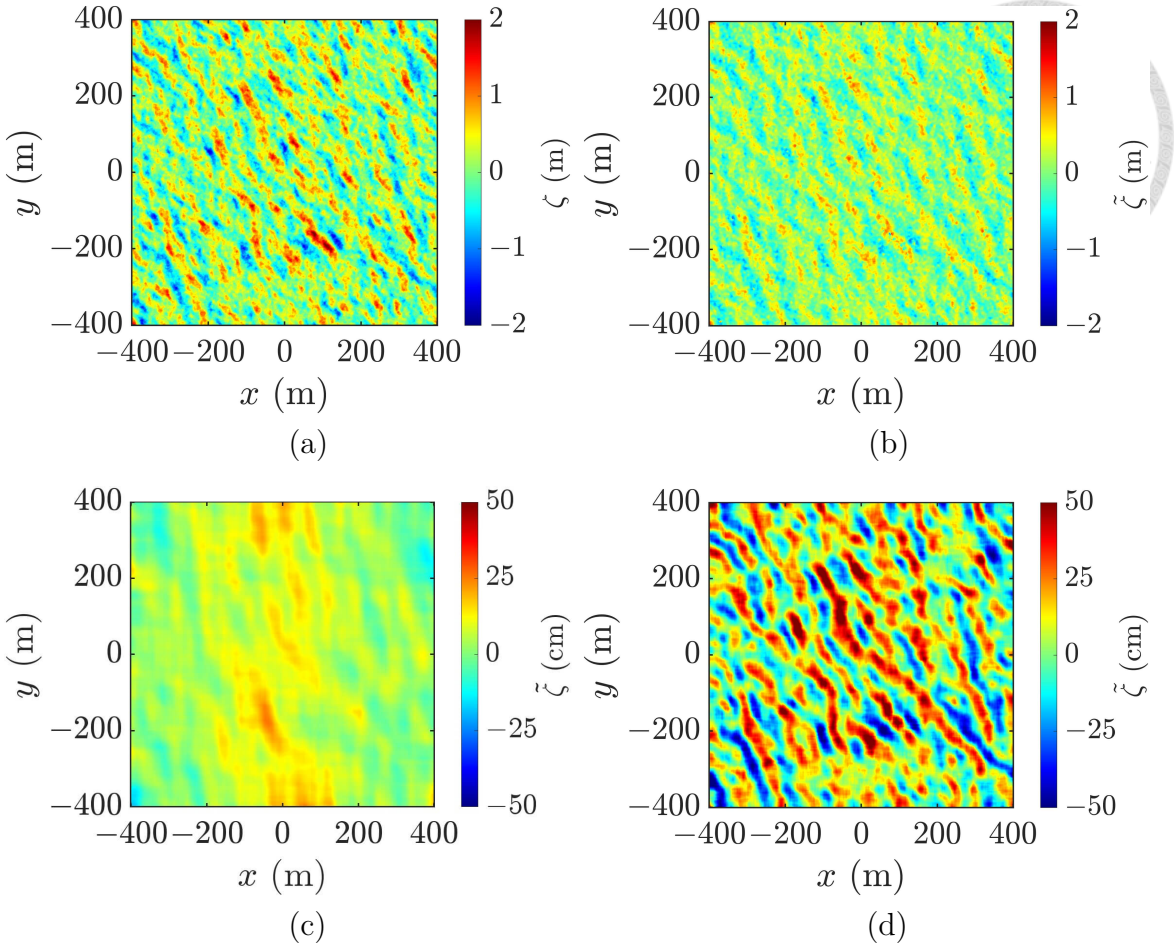

Figure 4.13: XTI-SAR images acquired from sea-surface profile of event 1 in Table 4.1, with default parameters in Table 4.2, $U_{10} = 9$ m/s, (a) simulated profile, (b) single pair, $w_x = w_y = 14$ m, RMSE = 26.89 cm, $\text{RMSE}_{\text{iw}} = 31.77$ cm, (c) single pair, $w_x = w_y = 202$ m, $\text{RMSE}_{\text{iw}} = 5.13$ cm, (d) 12 pairs, $w_x = w_y = 50$ m, $\text{RMSE}_{\text{iw}} = 22.37$ cm.

4.6 Detection of Subtle Internal-Wave Signatures

Finally, signatures of two subtle internal-wave events are reconstructed with the proposed imaging technique to demonstrate its merits. Fig.4.14(a) shows the sea-surface profile simulated with the parameter of event 2 in Table 4.1, with $U_{10} = 3$ m/s. The amplitude of internal-wave signatures is only 4 cm. Figs.4.14(b) and 4.14(c) show that the XTI-SAR image acquired with one pair of satellites fails to manifest the internal-wave signatures, even

doi:10.6342/NTU202501333

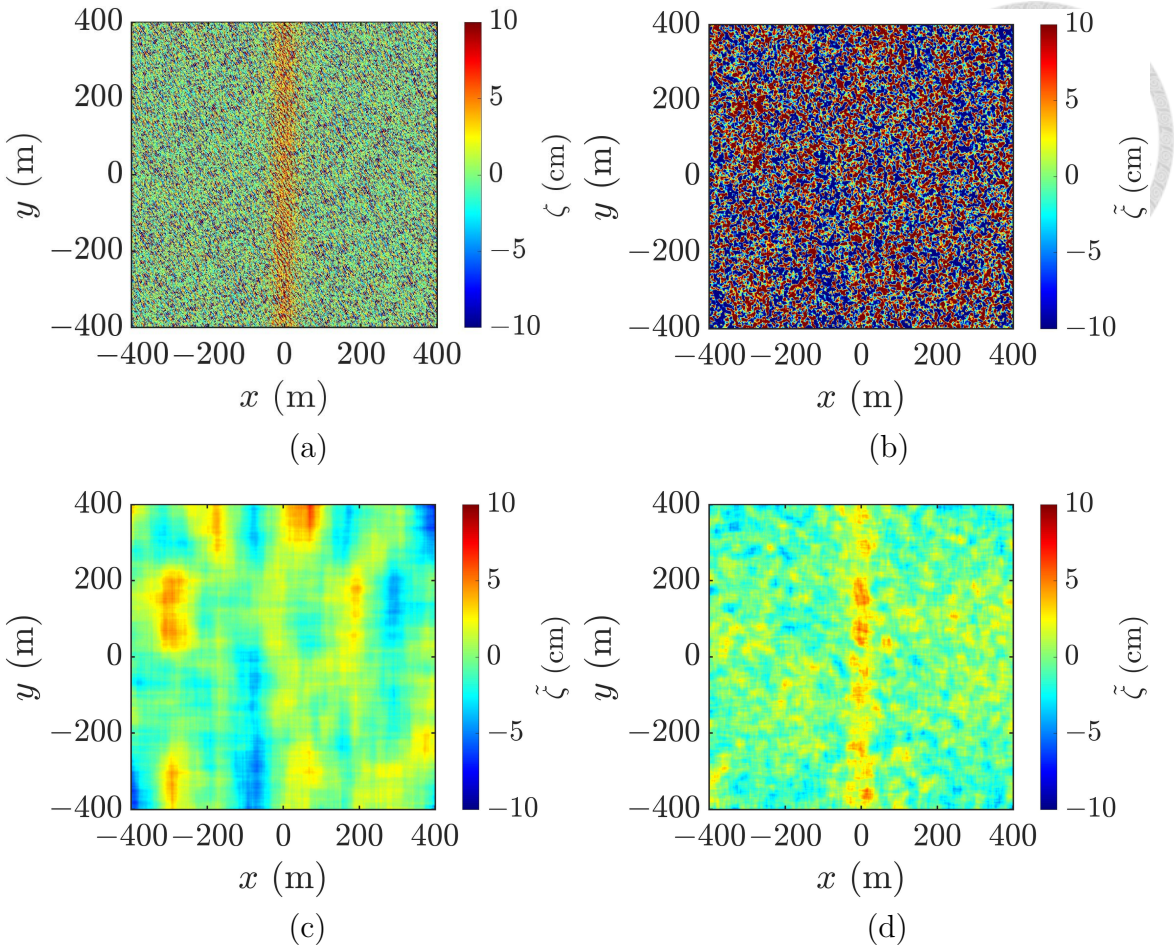

Figure 4.14: XTI-SAR images acquired from sea-surface profile of event 2 in Table 4.1, with default parameters in Table 4.2, $U_{10} = 3$ m/s, (a) simulated profile, (b) single pair, $w_x = w_y = 14$ m, RMSE = 13.79 cm, $\text{RMSE}_{\text{iw}} = 12.99$ cm, (c) single pair, $w_x = w_y = 202$ m, $\text{RMSE}_{\text{iw}} = 1.87$ cm, (d) 12 pairs, $w_x = w_y = 50$ m, $\text{RMSE}_{\text{iw}} = 1.32$ cm.

with large window size of $w_x = w_y = 202$ m. Fig.4.14(d) shows that the internal-wave signatures can be extracted with 12 pairs of satellites, followed by mean filter of size $w_x = w_y = 50$ m.

Internal-wave signatures with alternate polarity were observed on shoals of continental shelf [38]. Since a closed-form solution of internal wave is intractable, the parameters of event 2 in Table 4.1 are used to make an approximate solution, with one sech^2 function

doi:10.6342/NTU202501333

closely followed by another one with opposite polarity, given by

$$\eta(x,y,t) = \frac{\eta_0}{\sqrt{2}}\left\{\operatorname{sech}^2\left[\frac{(x-1.5\ell)\cos\phi_{\rm iw} + (y-1.5\ell)\sin\phi_{\rm iw} - c_{\rm iw}t}{1.8\ell}\right]\right.$$
$$\left.-\operatorname{sech}^2\left[\frac{(x+0.5\ell)\cos\phi_{\rm iw} + (y+0.5\ell)\sin\phi_{\rm iw} - c_{\rm iw}t}{\ell}\right]\right\} \tag{4.2}$$

which is substituted into (2.7) to derive the induced internal-wave signatures.

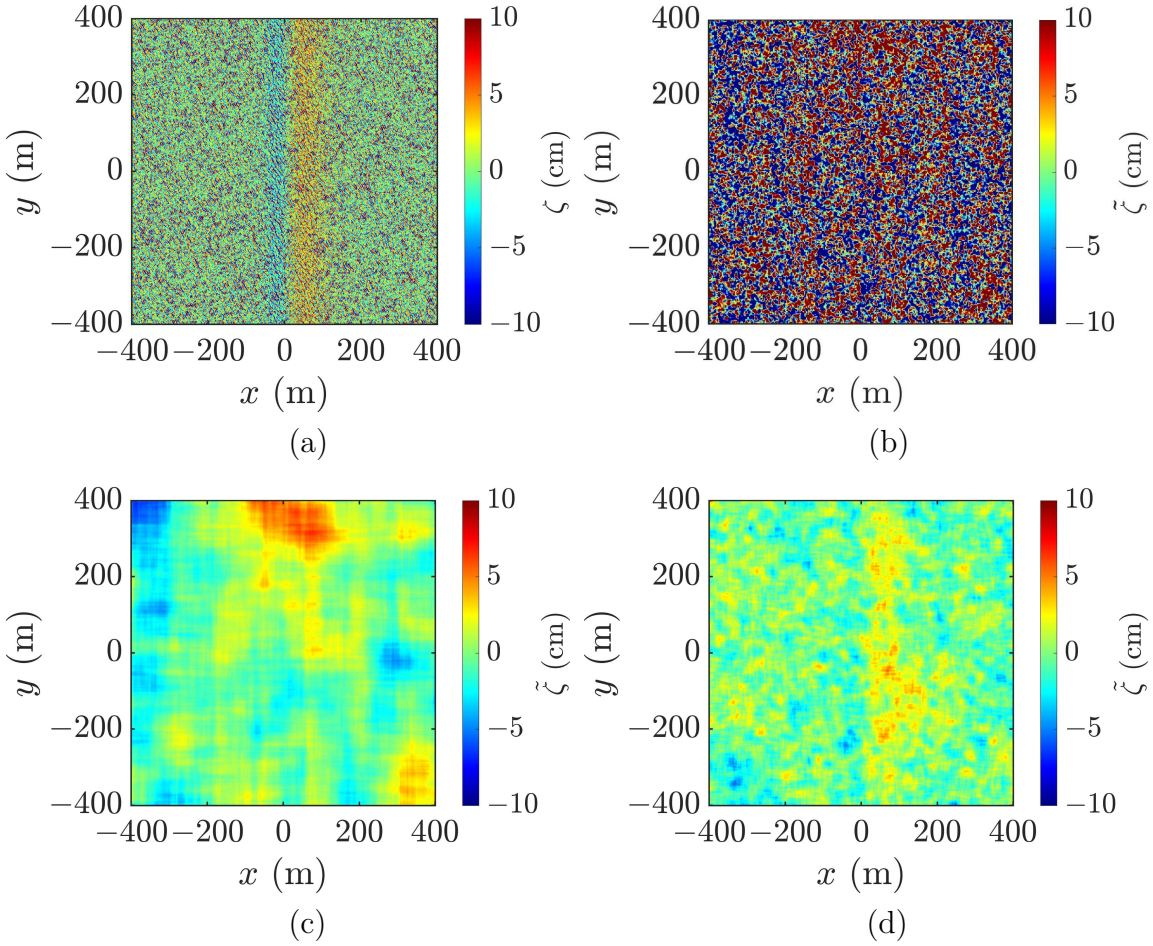

Figure 4.15: XTI-SAR images acquired from sea-surface profile of event 2 in Table 4.1, carrying internal-wave signatures of alternate polarity, with default parameters in Table 4.2, $U_{10} = 3$ m/s, (a) simulated profile, (b) single pair, $w_x = w_y = 14$ m, RMSE = 13.96 cm, $\text{RMSE}_{\rm iw} = 13.18$ cm, (c) single pair, $w_x = w_y = 202$ m, $\text{RMSE}_{\rm iw} = 1.99$ cm, (d) 12 pairs, $w_x = w_y = 50$ m, $\text{RMSE}_{\rm iw} = 1.30$ cm.

Fig.4.15(a) shows vague internal-wave signatures immersed in the wind wave. Fig.4.15(b)

doi:10.6342/NTU202501333

shows the XTI-SAR image acquired with single pair of satellites, followed by a mean filter of size $w_x = w_y = 14$ m. No internal-wave signatures are discernible. By applying mean filter of size $w_x = w_y = 202$ m, which worked well in previous cases, we obtain an ambiguous image in Fig.4.15(c).

Fig.4.15(d) shows the XTI-SAR image acquired with 12 pairs of satellites, followed by a mean filter of size $w_x = w_y = 50$ m. An alternate stripe-pattern becomes marginally discernible. This case suggests that fair horizontal resolution can help manifest subtle internal-wave signatures, for example, narrow stripe pattern with alternate polarity.

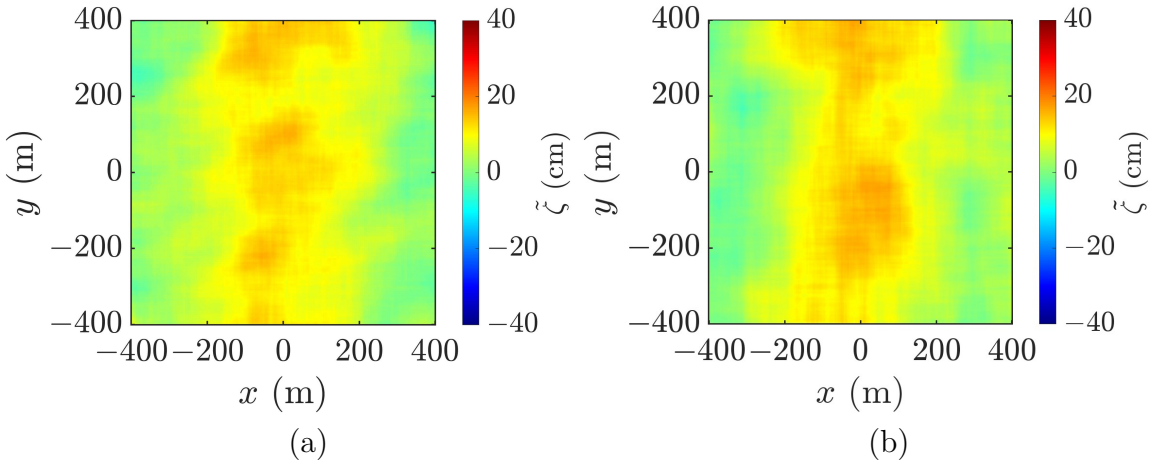

Figure 4.16: XTI-SAR images of sea-surface profile acquired with default parameters in Table 4.2 and $N_{wr} = 97$, $(w_x, w_y) = (194, 194)$ m, (a) without enhancing velocity bunching effect, RMSE = 9.32 cm, (b) with enhanced velocity bunching effect, RMSE = 9.36 cm.

Fig.4.16 shows that the RMSE value increases from 9.32 cm to 9.36 cm when the velocity bunching effect is enhanced and a large mean filter is exerted. The increment of RMSE value is 0.04 cm, smaller than the increment of 0.9 cm manifested in Fig.4.3 and 0.18 cm manifested

doi:10.6342/NTU202501333

in Fig.4.4, where one satellite pair is adopted and mean filter is not exerted.

It is also observed in Fig.4.10(c) that the RMSE is reduced from 26.3 cm to 9.32 cm by exerting large mean filter and adopting one satellite pair, is reduced to 10.2 cm by adopting multiple satellite pairs without exerting mean filter, and is further reduced to 8.82 cm by exerting large mean filter and adopting multiple satellite pairs. These reduced RMSE values are much larger than the increment attributed to the velocity bunching effect. Hence, the velocity bunching effect has little impact upon the proposed XTI-SAR imaging method.

doi:10.6342/NTU202501333

Chapter 5

Conclusions

An XTI-SAR imaging technique based on multiple satellite pairs is proposed to detect feeble internal-wave signatures immersed in wind-wave features. The radar echoed signals from simulated sea-surface profile are computed to test the efficacy of the proposed imaging method. The internal-wave signatures are manifested by processing echoed signals received by multiple satellite pairs, without deteriorating the horizontal resolution as in conventional methods that invoke mean filter. The XTI-SAR technique is immune to the blind-spot issue in detecting internal-wave signature with conventional SAR imaging methods. The joint effects of satellite-pair number, baseline and mean filter width on the height accuracy are analyzed by simulations under various wind speeds and three internal-wave events. The simulation results verify that the proposed method is capable of detecting internal-wave signatures with height accuracy of centimeters, at spatial resolution of 14 m, under wind speed of $U_{10} \leq 6$ m/s. The proposed method is capable of detecting narrow internal-wave signatures that

doi:10.6342/NTU202501333

cannot be identified with conventional methods invoking one pair of satellites.

doi:10.6342/NTU202501333

Bibliography

[1] M. Alford *et al.* "The formation and fate of internal waves in the South China Sea," *Nature*, vol. 521, no. 7550, pp. 65-69, May, 2015.

[2] X. Huang, Z. Chen, W. Zhao, Z. Zhang, C. Zhou, Q. Yang and J. Tian, "An extreme internal solitary wave event observed in the northern South China Sea," *Sci. Rep.*, vol. 6, no. 1, pp. 1–10, Jul. 2016.

[3] J. Li, Q. Zhang and T. Chen, "Numerical investigation of internal solitary wave forces on submarines in continuously stratified fluids," *J. Mar. Sci. Eng.*, vol. 9, no. 12, pp. 1–20, Dec. 2021.

[4] T. Wang, X. Huang, W. Zhao, S. Zheng, Y. Yang and J. Tian, "Internal solitary wave activities near the Indonesian submarine wreck site inferred from satellite images," *J. Mar. Sci. Eng.*, vol. 10, no. 2, pp. 1–12, Feb. 2022.

[5] T. Jia, J. Liang, X.-M. Li and K. Fan, "Retrieval of internal solitary wave amplitude in shallow water by tandem spaceborne SAR," *Remote Sens.*, vol. 11, no. 14, p. 1706, Jul.

doi:10.6342/NTU202501333

2019.

[6] X. Zhang, Z.-S. Wu and X. Su, "Electromagnetic scattering from deterministic sea surface with oceanic internal waves via the variable-coefficient Gardner model," *IEEE J. Sel. Top. Appl. Earth Observ. Remote Sens.*, vol. 11, no. 2, pp. 355-366, Feb. 2018.

[7] L. Ostrovsky and Y. Stepanyants, "Do internal solitons exist in the ocean?" *Revs. Geophys.*, vol. 27, no. 3, pp. 293–310, Aug. 1989.

[8] R. Romeiser and H. Graber, "Advanced remote sensing of internal waves by spaceborne along-track InSAR–A demonstration with TerraSAR-X," *IEEE Trans. Geosci. Remote Sens.*, vol. 53, no. 12, pp. 6735-6751, Dec. 2015.

[9] M. Zhang, J. Wang, Z. Li, K. Liang and X. Chen, "Laboratory study of the impact of the surface solitary waves created by the internal solitary waves on optical imaging," *J. Geophys. Res.: Oceans*, vol. 127, no. 2, pp. 1–17, Feb. 2022.

[10] F. Dias and A. Il'ichev, "Interfacial waves with free-surface boundary conditions: An approach via a model equation," *Phys. D, Nonlinear Phenomena*, vol. 150, nos. 3–4, pp. 278–300, Apr. 2001.

doi:10.6342/NTU202501333

[11] A. Santos-Ferreira, J. da Silva and J. Magalhaes, "SAR-mode altimetry observations of internal solitary waves in the tropical ocean Part 1: Case studies," *Remote Sens.*, vol. 10, no. 4, p. 644, Apr. 2018.

[12] C. Jackson and J. Apel. "Synthetic aperture radar marine user's manual," National Environmental Satellite, Data, and Information Service, Silver Spring, MD, USA, Tech. Rep., 2004, pp. 189 – 206. Accessed: Jun. 1, 2022. [Online]. Available: http://www.sarusersmanual.com

[13] J. Farrar, C. Zappa, R. Weller and A. Jessup, "Sea surface temperature signatures of oceanic internal waves in low winds," *J. Geophys. Res.*, vol. 112, no. C6, pp. 1–9, Jun. 2007.

[14] A. Donato, D. Peregrine and J. Stocker, "The focusing of surface waves by internal waves," *J. Fluid Mech.*, vol. 384, pp. 27–58, Apr. 1999.

[15] W. Kong, J. Chong and H. Tan, "Performance analysis of ocean surface topography altimetry by Ku-band near-nadir interferometric SAR," *Remote Sens.*, vol. 9, no. 9, p. 933, Sep. 2017.

[16] Q. Zheng, Y. Yuan, V. Klemas, and X. H. Yan, "Theoretical expression for an ocean internal soliton synthetic aperture radar image and determination of the soliton charac-

doi:10.6342/NTU202501333

teristic half width," *J. Geophys. Res., Oceans*, vol. 106, 867 no. C12, pp. 31415–31423, Dec. 2001.

[17] B. Liu, H. Yang, Z. Zhao, and X. Li, "Internal solitary wave propagation observed by tandem satellites," *Geophys. Res. Lett.*, vol. 41, no. 6, pp. 2077-2085, Mar. 2014.

[18] J. Magalhaes, I. Lapa, A. Santos-Ferreira, José da Silva, F. Piras *et al.* "Using a tandem flight configuration between Sentinel-6 and Jason-3 to compare SAR and conventional altimeters in sea surface signatures of internal solitary waves," *Remote Sens.*, vol. 15, no. 2, p. 392, Jan. 2023.

[19] P. Rosen, S. Hensley, I. Joughin, F. Li, S. Madsen, E. Rodriguez, and R. Goldstein, "Synthetic aperture radar interferometry," *Inverse Problems*, vol. 14, no. 4, pp. R1 – R54, Aug. 1998.

[20] M. Richards, "A beginner's guide to interferometric SAR concepts and signal processing," *IEEE A&E Syst. Mag.*, vol. 21, no.6, pp. 5-29, Jun. 2006.

[21] Z. Qiu, C. Ma, Y. Wang, F. Yu, C. Zhao, H. Sun, S. Zhao, L. Yang, J. Tang, and G. Chen, "Improving sea surface height reconstruction by simultaneous Ku- and Ka-band near-nadir single-pass interferometric SAR altimeter," *IEEE Trans. Geosci. Remote Sens.*, vol. 61, Art. no. 5209614, 2023.

doi:10.6342/NTU202501333

[22] S.-H. Hong, S. Wdowinski, F. Amelung, H.-C. Kim, J.-S. Won, and S.-W. Kim, "Using TanDEM-X pursuit monostatic observations with a large perpendicular baseline to extract glacial topography," *Remote Sens.*, vol. 10, no. 11, pp. 1–19, Nov. 2018.

[23] S. Leinss and P. Bernhard, "TanDEM-X: Deriving InSAR height changes and velocity dynamics of Great Aletsch Glacier," *IEEE J. Sel. Top. Appl. Earth Observ. Remote Sens.*, vol. 14, pp. 4798–4815, 2021.

[24] A. Elyouncha, L. Eriksson, R. Romeiser, and L. Ulander, "Measurements of sea surface currents in the Baltic Sea region using spaceborne along-track SAR," *IEEE Trans. Geosci. Remote Sens.*, vol. 57, no. 11, pp. 8584-8599, Nov. 2019.

[25] T. Farr *et al.*, "The shuttle radar topography mission," *Rev. Geophys.*, vol. 45, no. 2, May 2007, Art. no. RG2004.

[26] W. Kong, B. Liu, X. Sui, R. Zhang, and J. Sun, "Ocean surface topography altimetry by large baseline cross-interferometry from satellite formation," *Remote Sens.*, vol. 12, no. 21, p. 3519, Oct. 2020.

[27] H. Zhang, C. Fan, J. Meng, S. Li, and L. Sun, "Research on internal solitary wave detection and analysis based on interferometric imaging radar altimeter onboard the Tiangong-2 space laboratory," *Remote Sens.*, vol. 14, no. 1, p. 174, Dec. 2021.

doi:10.6342/NTU202501333

[28] R. Fjørtoft, J.-M. Gaudin, N. Pourthié, J.-C. Lalaurie, A. Mallet, J.-F. Nouvel, J. Martinot-Lagarde, H. Oriot, P. Borderies, C. Ruiz, and S. Daniel, "KaRIn on SWOT: Characteristics of near-nadir Ka-band interferometric SAR imagery," *IEEE Trans. Geosci. Remote Sens.*, vol. 52, no. 4, pp. 2172-2185, Apr. 2014.

[29] G. Chen, J. Tang, C. Zhao, S. Wu, F. Yu, C. Ma, Y. Xu, W. Chen, Y. Zhang, J. Liu, and L. Wu, "Concept design of the 'Guanlan' science mission: China's novel contribution to space oceanogrpahy," *Frontiers Mar. Sci.*, vol. 6, p. 194, Apr. 2019.

[30] X. Li and T. Yang, "A novel non-local denoising filter based on multibaseline InSAR," *IEEE J. Miniaturization Air Space Syst.*, vol. 4, no. 4, pp. 376-380, Dec. 2023.

[31] W. Zou, Y. Li, Z. Li and X. Ding, "Improvement of the accuracy of InSAR image co-registration based on tie points–a review," *Sensors*, vol. 9, no. 2, pp. 1259–1281, Feb. 2009.

[32] I. Kozlov, I. Kopyshov, D. Frey, E. Morozov, I. Medvedev, A. Shiryborova, K. P. Silvestrova, A. V. Gavrikov, E. A. Ezhova, D. M. Soloviev, E. V. Plotnikov, V. R. Zhuk, P. V. Gaisky, A. A. Osadchiev, and N. B. Stepanova, "Multi-sensor observations reveal large-amplitude nonlinear internal waves in the Kara Gates, Arctic Ocean," *Remote Sens.*, vol. 15, no. 24, p. 5769, Dec. 2023.

doi:10.6342/NTU202501333

[33] F. Liu, X. Fan, T. Zhang, and Q. Liu, "GNSS-based SAR interferometry for 3-D deformation retrieval: Algorithms and feasibility study," *IEEE Trans. Geosci. Remote Sens.*, vol. 56, no. 10, pp. 5736-5748, Oct. 2018.

[34] Z Wang, F. Liu, R. Shang, and J. Zhou, "A novel multiangle images association algorithm based on supervised areas for GNSS-based InSAR," *IEEE Geosci. Remote Sens. Lett.*, vol.20, Art. no. 4001705, 2023.

[35] A. Theodosiou, M. Kleinherenbrink, and P. López-Dekker, "Wide-swath ocean altimetry using multisatellite single-pass interferometry," *IEEE Trans. Geosci. Remote Sens.*, vol. 61, Art. no. 5210721, 2023.

[36] Starlink Coverage Tracker, Accessed: Apr. 12, 2024. [Online]. Available: https://starlink.sx

[37] P. Webb, "Introduction of Oceanography," Accessed: Dec. 8, 2024. [Online]. Available: https://rwu.pressbooks.pub/webboceanography.

[38] Z. Zhao, V. Klemas, Q. Zheng, and X.-H. Yan, "Satellite observation of internal solitary waves converting polarity," *Geophys. Res. Lett.*, vol.30, no. 19, p. 1988, Oct. 2003.

doi:10.6342/NTU202501333

[39] Y. Wei and L.-X. Guo, "Simulation of scattering on a time-varying sea surface beneath which an internal solitary wave travels," *Int. J. Remote Sens.*, vol. 38, no. 18, pp. 5251-5270, Sep. 2017.

[40] T. Kodaira, T. Waseda, M. Miyata, and W. Choi, "Internal solitary waves in a two-fluid system with a free surface," *J. Fluid Mech.*, vol. 804, pp. 201-223, Oct. 2016.

[41] L. Zou, Y. Hu, Z. Wang, Y. Pei, and Z. Yu, "Computational analyses of fully nonlinear interaction of an internal solitary wave and a free surface wave," *AIP Adv.*, vol. 9, no. 3, pp. 1–11, Mar. 2019.

[42] R. Romeiser, W. Alpers, and V. Wismann, "An improved composite surface model for the radar backscattering cross section of the ocean surface: 1. Theory of the model and optimization/validation by scatterometer data," *J. Geophys. Res., Oceans*, vol. 102, no. C11, pp. 25237-25250, Nov. 1997.

[43] R. Romeiser and W. Alpers, "An improved composite surface model for the radar backscattering cross section of the ocean surface: 2. Model response to surface roughness variations and the radar imaging of underwater bottom topography," *J. Geophys. Res., Oceans*, vol. 102, no. C11, pp. 25251-25267, Nov. 1997.

doi:10.6342/NTU202501333

[44] I. Robinson, *Measuring the Oceans From Space: The Principles and Methods of Satellite Oceanography*, Cham, Switzerland: Springer, 2004.

[45] W. Plant, "Bragg scattering of electromagnetic waves from the air/sea interface," *Surface Waves and Fluxes, vol. II, Remote Sensing*, G. Geemaert and W. Plant, Eds., Norwell, MA, USA: Kluwer, 1990, pp. 41–108.

[46] C. Mobley, *The Oceanic Optics Book*, Dartmouth, NS, Canada: International Ocean Colour Coordinating Group, 2022.

[47] T. Elfouhaily, B. Chapron, K. Katsaros and D. Vandemark, "A unified directional spectrum for long and short wind-driven waves," *J. Geophys. Res., Oceans*, vol. 102, no. C7, pp. 15781-15796, Jul.15, 1997.

[48] J. Smith, *Spectral audio signal processing*, Accessed: Oct. 11, 2023. [Online]. Available: https://ccrma.stanford.edu/%7Ejos/sasp/Practical_Zero_Padding.html

[49] B. Gutmann and H. Weber, "Phase unwrapping with the branch-cut method: Role of phase-field direction," *Appl. Opt.*, vol. 39, no. 26, pp. 4802-4816, Sep. 2000.

[50] M. Arevalillo-Herráez, F. Villatoro, and M. Gdeisat, "A robust and simple measure for quality-guided 2D phase unwrapping algorithms," *IEEE Trans. Image Proc.*, vol. 25, no. 6, pp. 2601-2609, Jun. 2016.

doi:10.6342/NTU202501333

[51] M. Arevalillo-Herráez, D. Burton, M. Lalor, and M. Gdeisat, "Fast two-dimensional phase-unwrapping algorithm based on sorting by reliability following a noncontinuous path," *Appl. Optics*, vol. 41, no. 35, pp. 7437-7444, Dec. 2002.

[52] D. Ghiglia and M. Pritt, *Two-dimensional Phase Unwrapping: Theory, Algorithms, and Software*, New York, NY, USA: Wiley, 1998.

[53] F. Gatelli, A. Monti-Guarnieri, F. Parizzi, P. Pasquali, C. Prati, and F. Rocca, "The wavenumber shift in SAR interferometry," *IEEE Trans. Geosci. Remote Sens.*, vol. 32, no. 4, pp. 855–865, Jul. 1994.

[54] A. Mestre-Quereda, J. Lopez-Sanchez, and J. Mallorqui, "Range spectral filtering in SAR interferometry: Methods and limitations," *Sensors*, vol. 22, no. 22, p. 8696, Nov. 2022.

[55] E. Rodriguez and J. Martin, "Theory and design of interferometric synthetic aperture radars," *IEE Proc. Radar Signal Process.*, vol. 139, no. 2, pp. 147–159, Apr. 1992.

[56] I. Cumming and F. Wong, *Digital Processing of Synthetic Aperture Radar Data*, Norwood, MA, USA: Artech House, 2005.

[57] T. Boyer, H. García, R. Locarnini, M. Zweng, A. Mishonov, J. Reagan, K. Weathers, O. Baranova, C. Paver, D. Seidov, and V. Igor. *World Ocean Atlas 2018: Density, NOAA*

doi:10.6342/NTU202501333

National Centers for Environmental Information Dataset. Accessed: Jun. 5, 2023. [Online]. Available: https://www.ncei.noaa.gov/archive/accession/NCEI-WOA18.

[58] J. Xue, H. Graber, B. Lund, and R. Romeiser, "Amplitudes estimation of large internal solitary waves in the Mid-Atlantic Bight using synthetic aperture radar and marine X-band radar images," *IEEE Trans. Geosci. Remote Sens.*, vol. 51, no. 6, pp. 3250-3258, Jun. 2013.

[59] G. Beutler, *Methods of Celestial Mechanics, I: Physical, Mathematical, and Numerical Principles*, 4th ed., Berlin, Germany: Springer, 2005.

[60] W. Alpers and C. Rufenach, "The effect of orbital motions on synthetic aperture radar imagery of ocean waves," *IEEE Trans. Antennas Propagat.*, vol. AP-27, no. 5, pp. 685–690, Sep. 1979.

[61] C. Rufenach and W. Alpers, "Imaging ocean waves by synthetic aperture radars with long integration times," *IEEE Trans. Antennas Propagat.*, vol. AP-29, no. 3, pp. 422–428, May 1981.

[62] W. Alpers, "Monte Carlo simulations for studying the relationship between ocean wave and synthetic aperture radar image spectra," *J. Geophys. Res., Oceans*, vol. 88, no. C3, pp. 1745–1759, Feb. 1983.

doi:10.6342/NTU202501333

[63] Q. Li, Y. Zhang, Y. Wang, Y. Bai, Y. Zhang and X. Li, "Numerical simulation of SAR image for sea surface," *Remote Sens.*, vol. 14, no. 3, p. 439, Jan. 2022.

[64] K. Hasselmann, R. Raney, W. Plant, W. Alpers, R. Shuchman, D. Lyzenga, C. Rufenach, and M. Tucker, "Theory of synthetic aperture radar ocean imaging: A MARSEN view," *J. Geophys. Res., Oceans*, vol. 90, no. C3, pp. 4659-4686, May 1985.

[65] K. Hasselmann and S. Hasselmann, "On the nonlinear mapping of an ocean wave spectrum into a synthetic aperture radar image spectrum and its inversion," *J. Geophys. Res., Oceans*, vol. 96, no. C6, pp. 10713-10729, Jun.15, 1991.

doi:10.6342/NTU202501333

Appendix: Registration Error Induced by Target Motion

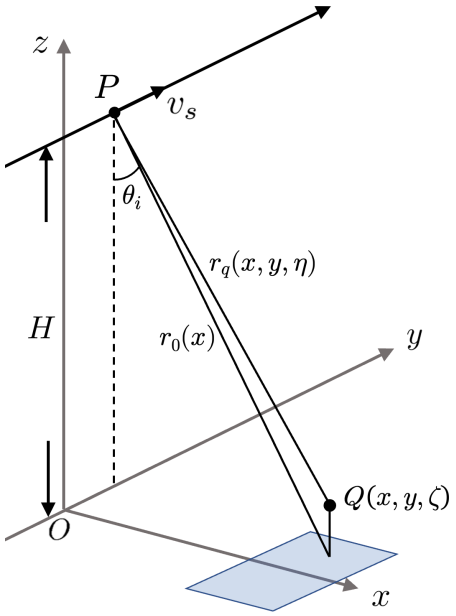

Figure I.1: Schematic of slant range between satellite P and a moving target Q.

Fig.I.1 shows a schematic of slant range between satellite P and a moving target Q. The satellite P flies in y direction at speed v_s, and the moving point target Q is located at (x, y, ζ). The origin is set to the nadir point of the satellite when $\eta = 0$, the z-axis points upwards, and the x-axis is along the ground range direction of the satellite. Pulses are emitted from the satellite at an incident angle θ_i, and the squint angle is set to zero for simplicity. The

doi:10.6342/NTU202501333

point target Q marks the sea surface at horizontal coordinates (x, y), and moves up and down in z direction with slow time η. The height of Q is approximated as

$$\zeta(x, y, \eta) \simeq \zeta_c + v_\zeta(\eta - \eta_c) \tag{I.1}$$

where $\zeta_c = \zeta(x, y, \eta_c)$, $\eta_c = y/v_s$ is the beam-crossing time of Q, and the change rate of surface height is approximated as

$$v_\zeta = \frac{\zeta(x, y, T_a/2) - \zeta(x, y, -T_a/2)}{T_a} \tag{I.2}$$

Thus, the slant range $r_q(x, y, \eta)$ between P and Q can be represented as

$$\begin{aligned} r_q(x, y, \eta) &= \left|\overline{PQ}(\eta)\right| \\ &= \left\{x^2 + (y - \eta v_s)^2 + [\zeta(x, y, \eta) - H]^2\right\}^{1/2} \\ &= \left\{x^2 + H^2 - 2H\zeta_c + \zeta_c^2 + (2\zeta_c v_\zeta - 2Hv_\zeta)(\eta - \eta_c) + (v_s^2 + v_\zeta^2)(\eta - \eta_c)^2\right\}^{1/2} \\ &\simeq \left\{x^2 + H^2 + \left[\left(y + \frac{Hv_\zeta}{v_s}\right) - \eta v_s\right]^2\right\}^{1/2} \end{aligned} \tag{I.3}$$

where $v_\zeta \ll v_s$ and $\zeta_c \ll H$. The slant range $r_q(x, y, \eta)$ is the same as that between P and a stationary target located at $(x, y', 0)$, with

$$y' = y + \frac{Hv_\zeta}{v_s} = y + \frac{r_0(x)v_r}{v_s} \tag{I.4}$$

where $r_0(x) = \sqrt{x^2 + H^2}$ and $v_r = v_\zeta \cos\theta_i$ is the component of v_ζ in the radar pointing direction. The expression in (I.4) is consistent with its counterparts in [60]-[65].

doi:10.6342/NTU202501333

In [60], the phase shift incurred by ocean wave movement was derived to reveal discrepancy between apparent azimuth position and true azimuth position of a point on the surface, and degradation in azimuth resolution was also predicted in the theoretical power density. In [61], ensemble average of SAR image density distribution was computed to investigate the modulation of ocean wave on SAR images. The expression of azimuth position is compatible to that in eqn.(I.4). The result was cited in [62] to investigate the relationship between SAR image and ocean wave spectrum in simulating NRCS of 1D ocean surface profile, and cited in [63] to simulate SAR images of moving ocean waves. In [64], velocity bunching effect was considered in SAR imaging of ocean wave, where a linear modulation transfer function (MTF) could be used to map an ocean wave spectrum to its corresponding SAR image under certain condition. In [65], the ocean surface motion was specified by imposing azimuthal displacement upon a frozen image via an expression similar to eqn.(I.4), and degradation in azimuth resolution was manifested.

doi:10.6342/NTU202501333